



Interstellar Polarization Survey. V. Galactic Magnetic Field Tomography of the Spiral Arms Using Optical and Near-infrared Starlight Polarization

Downloaded from: <https://research.chalmers.se>, 2026-05-09 21:32 UTC

Citation for the original published paper (version of record):

Angarita Arenas, Y., Versteeg, M., Haverkorn, M. et al (2025). Interstellar Polarization Survey. V. Galactic Magnetic Field Tomography of the Spiral Arms Using Optical and Near-infrared Starlight Polarization. *Astronomical Journal*, 170(1).
<http://dx.doi.org/10.3847/1538-3881/addecc>

N.B. When citing this work, cite the original published paper.



Interstellar Polarization Survey. V. Galactic Magnetic Field Tomography of the Spiral Arms Using Optical and Near-infrared Starlight Polarization

Y. Angarita^{1,2} , M. J. F. Versteeg¹ , M. Haverkorn¹ , V. Pelgrims³ , C. V. Rodrigues⁴ , A. M. Magalhães⁵ ,
R. Santos-Lima⁵ , and Koji S. Kawabata⁶

¹ Department of Astrophysics/IMAPP, Radboud University, PO Box 9010, 6500 GL Nijmegen, The Netherlands; y.angarita@astro.ru.nl,
yenifer.angarita@chalmers.se

² Department of Space, Earth & Environment, Chalmers University of Technology, 412 93 Gothenburg, Sweden

³ Université Libre de Bruxelles, Science Faculty CP230, B-1050 Brussels, Belgium

⁴ Divisão de Astrofísica, Instituto Nacional de Pesquisas Espaciais (INPE/MCTI), Av. dos Astronautas, 1758, São José dos Campos, SP, Brazil
⁵ IAG, Universidade de São Paulo, Brazil

⁶ Hiroshima Astrophysical Science Center, Hiroshima University, Kagamiyama, Higashi-Hiroshima, Hiroshima 739-8526, Japan

Received 2024 November 11; revised 2025 May 11; accepted 2025 May 28; published 2025 June 27

Abstract

Interstellar linear polarization occurs when starlight passes through elongated dust grains aligned by interstellar magnetic fields. The observed polarization can come from different dust structures along the line of sight (LOS). By combining polarization measurements with stellar distances, we can study the plane-of-sky Galactic magnetic field (GMF) between the observer and the star and separate the contributions of clouds with different GMF properties. We used optical and near-infrared (NIR) polarization data from three regions in the Galactic plane ($|b| < 1^\circ$ and $19.8 < l < 25.5$) to perform a polarization decomposition across the Galactic arms. A comparison between the optical and NIR data showed an optical-to-NIR polarization ratio of two to three along the LOS and a consistent polarization angle across both wavelengths in all studied regions, within the measurement uncertainties. We applied the Bayesian Inference of Starlight Polarization in one dimension and the Gaussian mixture model methods to decompose the polarization in the three regions. The optical and NIR observations complemented each other, consistently identifying nearby ($d \lesssim 143$ pc), intermediate (0.47 kpc $< d < 1.2$ kpc), and distant (1.5 kpc $< d < 2.5$ kpc) polarizing clouds, in agreement with previous findings of the Local Bubble wall, the Local Arm, and Sagittarius Arm dust structures. The results from both polarization decomposition methods agree and complement each other. Polarization tomography revealed significant LOS variations in the plane-of-sky magnetic field orientation in two of the three regions. The relative alignment between the magnetic fields traced by starlight polarization and Planck's polarized thermal dust emission at 353 GHz reaffirmed these variations.

Unified Astronomy Thesaurus concepts: [Starlight polarization \(1571\)](#); [Interstellar medium \(847\)](#); [Interstellar magnetic fields \(845\)](#); [Milky Way magnetic fields \(1057\)](#); [Galaxy structure \(622\)](#)

1. Introduction

Linear starlight polarization is produced in the interstellar medium (ISM) when unpolarized light from stars is scattered by elongated dust grains aligned with the Galactic magnetic field (GMF; J. S. Hall 1949; W. A. Hiltner 1949). The direction of the linear polarization indicates the magnetic field orientation on the plane of the sky, while the intensity is associated with the amount of polarizing dust and the magnetic field's inclination relative to the line of sight (LOS; K. Serkowski 1962). Therefore, starlight polarization provides insights into the plane-of-sky magnetic field component and dust properties along the LOS up to the position of the stars.

The magnetized ISM is a dynamic and heterogeneous environment where the properties of dust and magnetic field vary spatially (e.g., see K. Ferrière 2015; M. Haverkorn 2015, and references therein). Consequently, the observed starlight polarization may contain contributions of multiple structures characterized by distinct magnetic field and dust properties (see, e.g., G. V. Panopoulou et al. 2019). When combined with accurate stellar distance measurements, starlight polarization

becomes a powerful tool for localizing and characterizing the different magnetized dust structures found between the observer and the star.

Starlight polarization has been used alongside stellar distance measurements to study structures in the ISM and large-scale GMF (e.g., S. Lloyd & M. O. Harwit 1973; L. A. Fowler & M. Harwit 1974; R. S. Ellis & D. J. Axon 1978; C. Heiles 1996; P. Fosalba et al. 2002; A. Berdyugin et al. 2014; M. J. F. Versteeg et al. 2023). For example, J. L. Leroy (1999) combined interstellar dust polarization and Hipparcos parallaxes to estimate the distance to the Local Bubble wall, revealing its irregular shape, with the nearest boundary around 70 pc and the farthest extending beyond 150 pc. More recently, the development of accurate stellar distance catalogs (e.g., C. A. L. Bailer-Jones et al. 2021; F. Anders et al. 2022) and three-dimensional (3D) dust extinction maps (e.g., D. Lenz et al. 2017; G. M. Green et al. 2019; R. H. Leike et al. 2020; R. Lallement et al. 2022; J. L. Vergely et al. 2022; G. Edenhofer et al. 2024), based on precise parallax and photometry observations from the Gaia satellite (Gaia Collaboration et al. 2018, 2021), has led to advancements in investigating the 3D magnetic field structure in the Galaxy. For instance, G. V. Panopoulou et al. (2019) demonstrated the feasibility of tomographic reconstruction of the interstellar magnetic field using stellar distance, H I emission spectra, and R-band starlight polarization.



Original content from this work may be used under the terms of the [Creative Commons Attribution 4.0 licence](#). Any further distribution of this work must maintain attribution to the author(s) and the title of the work, journal citation and DOI.

Investigating the 3D structure of the GMF at both small and large scales enables us to understand the dynamics of important processes in the ISM, such as the formation and evolution of structures (e.g., see K. Pattle et al. 2023), the propagation of charged particles (e.g., R. Beck 2003), and the magnetic field’s contributions to turbulence and gas dynamics (e.g., see A. Beresnyak & A. Lazarian 2019). Models and observations suggest that the large-scale GMF follows the shape of the spiral arms, thereby aligning nearly parallel to the Galactic thin disk (R. Beck 2003; K. Ferrière 2015; M. Havekorn 2015), while our understanding of the GMF in interarm regions remains limited. Starlight polarization data generally confirm this alignment (P. Fosalba et al. 2002; S. Nishiyama et al. 2009; D. P. Clemens et al. 2020) and can test large-scale GMF models (M. D. Pavel et al. 2012; M. D. Pavel 2014). Moreover, starlight polarization orientations probe the local plane-of-sky direction of the GMF along the Galactic arms (A. Berdyugin et al. 1995; C. Heiles 1996). On smaller scales, the GMF properties vary significantly, particularly in regions of high column density (J. D. Soler et al. 2016; K. Pattle et al. 2023). However, in the nearby diffuse ISM, the small-scale magnetic field appears to align with the structure of the large-scale GMF (Y. Angarita et al. 2024). Furthermore, polarization efficiency analyses further reveal that the turbulent, or random, component of the magnetic field may dominate over the regular, ordered component (H. Hatano et al. 2013).

Many polarization tomography techniques have been developed, providing insights into the 3D structure of the GMF at different scales (e.g., M. D. Pavel 2014; I. Medan & B. G. Andersson 2019; G. V. Panopoulou et al. 2019; V. Pelgrims et al. 2023, 2024; Y. Doi et al. 2024; M. J. F. Versteeg et al. 2024). For example, Y. Doi et al. (2024) probed multiple polarizing clouds in the Sagittarius Arm between 1.23 and 2.23 kpc, using *R*-band polarization. The study revealed different magnetic field orientations deviating notably from the direction parallel to the Galactic thin disk (i.e., 90°). Furthermore, B. G. Andersson & S. B. Potter (2005) and M. J. F. Versteeg et al. (2024) examined the magnetic field properties of the Coalsack region, located about 200 pc away, using optical polarization. They found that, in addition to the polarization caused by the Coalsack cloud, the farthest stars revealed a second polarizing cloud roughly between 1.3 and 1.5 kpc, likely in the Carina–Sagittarius spiral arm. Finally, N. Uppal et al. (2024) found signatures of the Local Arm, the Perseus Arm, and the Outer Arm using optical linear polarization data of open clusters toward the Galactic anticenter.

In this work, we present a tomographic analysis of the GMF across the spiral arms, from the Local Bubble wall to the Sagittarius Arm. To this end, we use optical and near-infrared (NIR) starlight polarization observations from the Interstellar Polarization Survey (IPS; A. M. Magalhães et al. 2005) and the Galactic Plane Infrared Polarization Survey (GPIPS; D. P. Clemens et al. 2012), respectively. In Section 2, we present the polarization catalogs and ancillary data, such as distance and 3D dust maps, used for the analysis. In Section 3, we introduce the polarization decomposition methods used in the tomography analysis. We describe our results in Section 4, starting with a comparison between optical and NIR polarization observations, followed by the results of the magnetic field tomography. We discuss these results in Section 5, comparing them with previous findings for similar regions, and present our conclusions and summary in Section 6.

2. Polarization and Ancillary Data

We use three regions, identified as C5, C45, and C50, from IPS observations (A. M. Magalhães et al. 2005 and A. M. Magalhães et al. 2025, in preparation), which are located within the Galactic thin disk at $-1^\circ < b < 1^\circ 3$ and $20^\circ 0 < l < 25^\circ 5$ (Figure 1). These regions, with an area of $0^\circ 3 \times 0^\circ 3$ each, were chosen for their low Galactic latitude, their proximity in the sky, and the large number of objects with optical and NIR polarization observations, all of which facilitate a multiwavelength polarization study of the Galactic arms. The following sections describe the starlight polarization observations in the *V* band and *H* band used in our study, along with the ancillary data. Additionally, we outline the quality filters and preprocessing steps employed to prepare our data sets for analysis.

2.1. Optical Polarization Data

The *V*-band polarization data were extracted from the IPS-GI catalog (M. J. F. Versteeg et al. 2023). The *V*-band photometric and polarimetric parameters were processed using the SOLVEPOL pipeline (E. A. Ramírez et al. 2017). The catalog includes relevant parameters such as the 84th, 50th, and 16th percentiles of the optical extinction posterior distributions (F. Anders et al. 2022), and the unique Gaia EDR3 source identifier (Gaia Collaboration et al. 2021).

We kept optical polarization measurements with a signal-to-noise ratio (SNR) above three, as we aim to retain nearby low-polarization values often discarded by higher SNR cuts (Y. Angarita et al. 2023; M. J. F. Versteeg et al. 2023). At $\text{SNR} > 3$, the degree of polarization measured may be affected by Ricean bias (e.g., E. A. Ramírez et al. 2017). Therefore, we debiased the polarization degree with the generalized modified asymptotic estimator of S. Plaszczyński et al. (2014):

$$p_{v,d} = p_v - \sigma_{p_v}^2 \frac{1 - e^{-p_v^2/\sigma_{p_v}^2}}{2p_v}, \quad (1)$$

where $p_{v,d}$ is the debiased polarization, p_v is the observed polarization degree, and σ_{p_v} is its uncertainty.

We do not correct for the estimated instrumental polarization of 0.07% since it is below the median fractional polarization error measured (see M. J. F. Versteeg et al. 2023, for more details). Furthermore, following the quality filters suggested by M. J. F. Versteeg et al. (2023), we excluded stars with $\sigma_{p_v} > 0.8\%$ to avoid untrustworthy polarization values. Additionally, we discarded the duplicates generated during the crossmatch with the Gaia EDR3 catalog (Gaia Collaboration et al. 2021); see details in M. J. F. Versteeg et al. (2023). The optical polarization maps of each region are presented in Figure 1 (the white pseudovectors).

2.2. Near-infrared Polarization Data

We use NIR polarization observations in the *H* band ($1.6 \mu\text{m}$) from GPIPS Data Release 4 presented by D. P. Clemens et al. (2020). We queried the GPIPS catalog through the table access protocol VizieR service.⁷ We selected rectangular regions centered in the IPS-GI fields, each with twice the size of the IPS-GI field of view, i.e., $0^\circ 6 \times 0^\circ 6$. GPIPS observations surveyed Galactic latitudes between -1° and $+1^\circ$. As a result,

⁷ <https://tapvizier.u-strasbg.fr/adql/?J/ApJS/249/23>

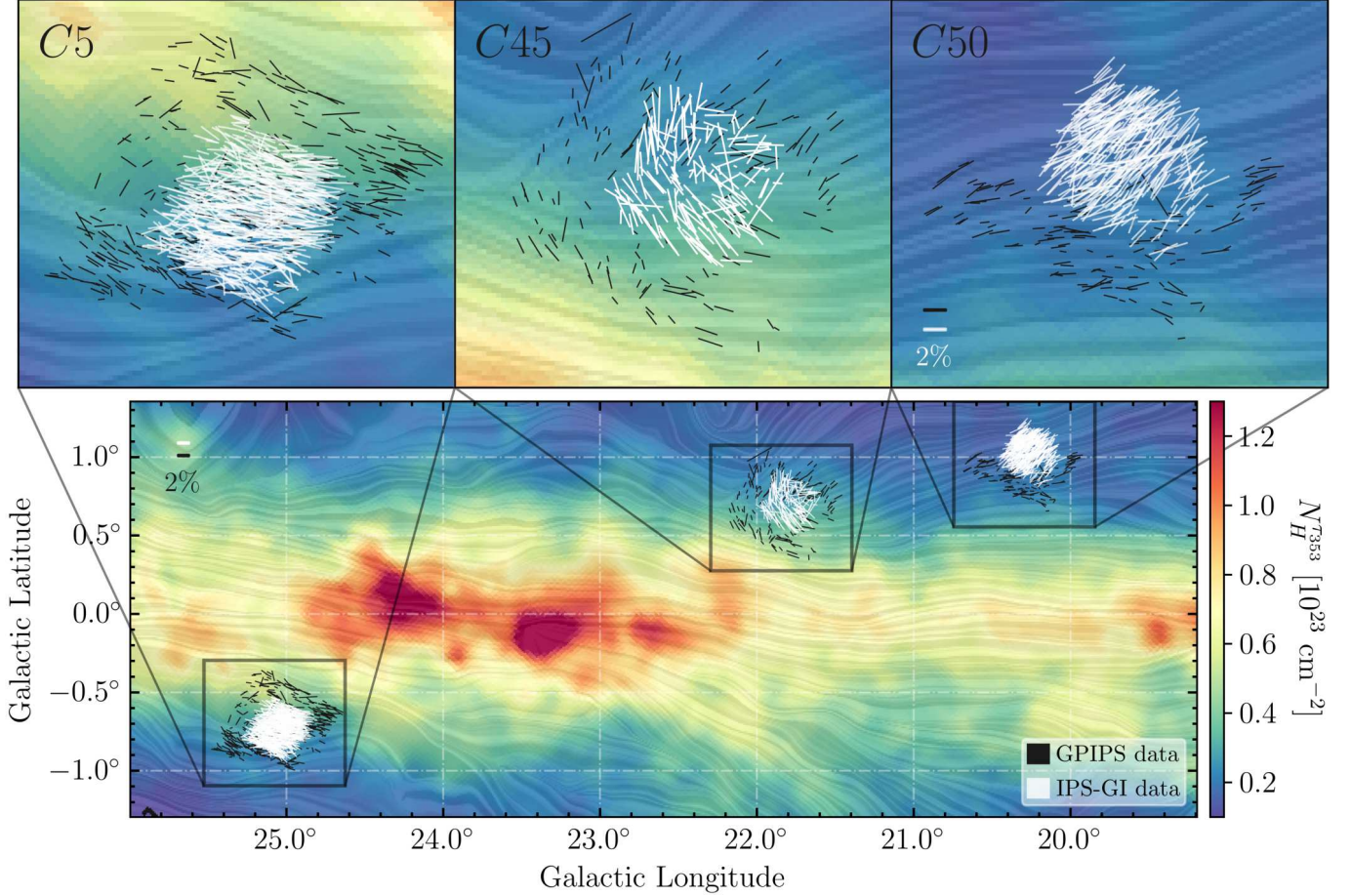


Figure 1. Starlight polarization observations from IPS-GI (in white) and GPIPS (in black) catalogs, after filtering, in the regions C5, C45, and C50. The colored background is the column density obtained using the thermal dust optical depth maps at 353 GHz from Planck Collaboration Int. XLVIII et al. (2016). The white texture in the background represents the plane-of-sky GMF orientation as observed by Planck (Planck Collaboration XII et al. 2020), and it is generated using line integral convolution (LIC, B. Cabral & L. Leedom 1993).

the IPS-GI region C50 is covered only partially by the NIR polarization catalog.

The H -band polarization degree is already debiased in D. P. Clemens et al. (2020) following

$$p_{h,d} = \sqrt{p_h^2 - \sigma_{p_h}^2}, \quad (2)$$

where σ_{p_h} is the polarization degree uncertainty. We kept the NIR polarization SNR above three. Additionally, we filtered the GPIPS data set by the magnitude and polarization uncertainties, retaining bright stars with $m_h < 12.5$ mag and $\sigma_{p_h} < 2\%$, as suggested by D. P. Clemens et al. (2020).

We converted the normalized Stokes parameters $q_h^{\text{eq}} = (Q_h/I_h)_{\text{eq}}$ and $u_h^{\text{eq}} = (U_h/I_h)_{\text{eq}}$ in the equatorial reference frame to the International Astronomical Union (IAU) Galactic reference frame, i.e., q_h^{gal} and u_h^{gal} , to facilitate the analysis and comparison with optical polarization. From here on, we will refer to the fractional Stokes parameters in Galactic coordinates as q_h and u_h for simplicity. The NIR polarization maps of each region are presented in Figure 1 (the black pseudovectors).

2.3. Parallax and Photogeometric Distance

We crossmatched the IPS-GI and GPIPS data sets separately with the Gaia EDR3 catalog (Gaia Collaboration et al. 2021) to

obtain the renormalized unit weight error (RUWE; which indicates the goodness of the astrometric solution), the parallax (ϖ), and photometry parameters, along with their uncertainties. We employ Gaia’s parameters to define quality filters when using parallax measurements. We also crossmatched the individual polarization data sets with the C. A. L. Bailer-Jones et al. (2021) distance catalog to obtain the median stellar photogeometric distance, including the 84th (high) and 16th (low) posterior percentiles.

The catalogs were crossmatched using the unique Gaia EDR3 source identifier. In the case of the GPIPS data set, we also used the precomputed crossmatched catalog available in Gaia’s archive to relate the source identifier of Gaia Data Release 2 to Gaia EDR3. The reliability of the Gaia parameters, including the photogeometric distance, is assessed with the parallax SNR, ϖ/σ_ϖ , and the RUWE value associated with each Gaia source. We adopted $\varpi/\sigma_\varpi > 2$ and $\text{RUWE} < 1.4$, as suggested in Gaia Collaboration et al. (2021), Gaia Collaboration et al. (2023), and C. A. L. Bailer-Jones et al. (2021).

2.4. Crossmatching Polarization Data Sets

Next, we crossmatched the IPS-GI data sets with the GPIPS data sets using the unique Gaia EDR3 source identifier. We relaxed the NIR polarization SNR filter to two for C45 and C50 due to the limited number of common stars available for

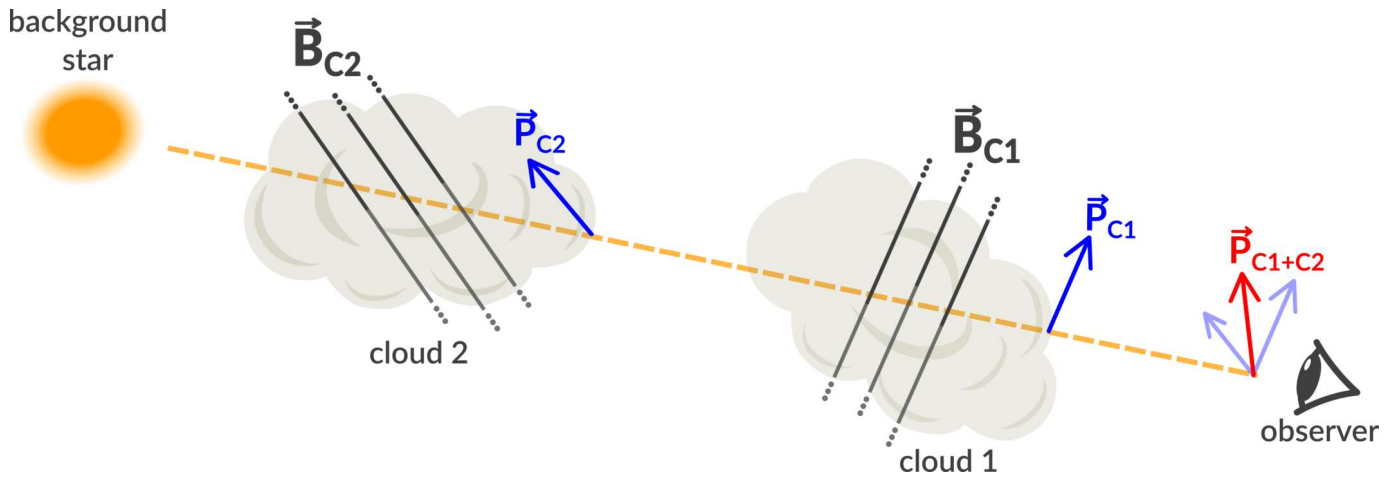


Figure 2. Illustration of the observed starlight polarization produced by two clouds with different magnetic field properties.

analysis. The crossmatched data set ended up with 47, 26, and 12 measurements in the regions of C5, C45, and C50, respectively, after filtering. The small number of common stars in C50 is due to GPIPS only partially covering the IPS-GI region. Therefore, the statistical results are less robust in this area than in the other two regions, which have more measurements.

2.5. Non-interstellar-medium Polarization

Despite the quality filters applied (Sections 2.1 and 2.2), atypical polarization measurements may remain. These observations may be caused by intrinsically polarized sources. Additionally, in the case of IPS-GI data, odd polarization measurements might be due to mismatches or superposition of the ordinary and extraordinary images created by the Savart prism in a crowded field of view (A. M. Magalhães et al. 2005; M. J. F. Versteeg et al. 2023).

To remove potential non-ISM polarization, we analyzed the correlation of the distributions of the normalized Stokes parameters q and u with distance and performed a sigma clipping on atypical values. We adopted the method from V. Pelgrims et al. (2024) as follows. First, we defined a set of nearby neighbors for each data point in a 3D spatial reference frame, typically between 10 and 15, depending on the number of measurements available for the region. Then, we computed the mean of the q and u measurements and the covariance matrix from their uncertainties, respectively, for each group of neighbors. We did not consider distance uncertainties here. Subsequently, we evaluated the deviations of each data point from the neighborhood mean value, weighting by the uncertainties (Equation (8) from V. Pelgrims et al. 2024). Finally, we removed values with deviations above a 3σ threshold.

In the data processing for the decomposition with Bayesian Inference of Starlight Polarization in one dimension (BISP-1; Section 3.1), we utilized the inverse parallax in the sigma clipping, while for the clustering analysis (Section 3.2), we employed photogeometric distances. Furthermore, we did not apply sigma clipping to the crossmatched polarization data sets (Section 2.4) due to the limited number of common stars in each region.

2.6. Three-dimensional Dust Maps of the Local Galaxy

We use 3D dust maps from J. L. Vergely et al. (2022) to track and compare the possible origin of the starlight polarization within large-scale dust structures along the sight lines. We retrieved the 3D maps through the G-Tomo platform⁸ using the central coordinates of the IPS-GI fields. Since GPIPS data span a wide range of distances, we use 3D dust maps with resolutions of 10 pc, 25 pc, and 50 pc, extending to radii of ~ 1.5 kpc, ~ 3 kpc, and ~ 5 kpc, respectively. The low-resolution maps often contain significant uncertainties, especially at large distances. Therefore, the dust structures interpretation must be done with caution.

3. Starlight Polarization Tomography

The starlight polarization carries information of the plane-of-sky magnetic field component and dust properties of the ISM between the observer and the star (J. S. Hall 1949; W. A. Hiltner 1949; K. Serkowski 1962). This signal can include contributions from distinct dust structures with varying magnetic field properties, as illustrated in Figure 2. The variations in magnetic field and dust properties along the LOS are reflected in changes in the normalized Stokes parameters $q = Q/I$ and $u = U/I$, as a function of distance (e.g., see G. V. Panopoulou et al. 2019; V. Pelgrims et al. 2023; Y. Doi et al. 2024). In the following section, we present two methods that use stellar polarization and distance information to localize and characterize the main polarizing screens along the LOS.

3.1. Bayesian Approach to Find Polarizing Screens

BISP-1⁹ (V. Pelgrims et al. 2023) performs a tomographic decomposition of the plane-of-sky magnetic field properties in the ISM along the LOS. BISP-1 models dust clouds as thin polarizing layers that independently contribute to the total observed polarization of background stars. Thus, it looks for changes in the Stokes parameters q and u as a function of distance obtained from the parallax.

This Bayesian method considers all sources of uncertainty in the data and modeling. It accounts for uncertainties in the stellar parallax, assessing the probability of stars being in front

⁸ <https://explore-platform.eu/sdas>

⁹ https://github.com/vpelgrims/BISP_1/

or behind a polarizing cloud, thereby determining its polarization properties (V. Pelgrims et al. 2023). To this end, it uses the Gaussian nature of the parallax errors. Furthermore, the approach considers the polarization covariance matrix Σ_i of the i th measurement as the combination of the intrinsic scatter, C_{int} , primarily attributed to ISM turbulence, and the observational errors, C_{obs} . If the star is in the foreground of all the clouds, then the polarization is assumed to be zero, and the uncertainty is only due to the observational errors.

We tested models with one to five polarizing layers for each data set considered. We used the Akaike information criterion (AIC; H. Akaike 1998) to identify the model that minimizes the loss of information. The AIC uses the maximized value of the likelihood function and the number of parameters to balance the goodness of the model fit with the complexity of the model, penalizing complex models to avoid overfitting.

The solution provided posterior distributions of the distance, Stokes parameters, and elements of the covariance (C_{int}) for each cloud, obtained after 40,000 nested sampling iterations (see V. Pelgrims et al. 2023, for more details). We calculated the polarization degree and orientation posteriors from the cumulative posterior of $q_{(v, h)}$ and $u_{(v, h)}$. From these posteriors and their spread, we derive the mean and median values, along with uncertainties, for the distance, polarization degree, and orientation.

BISP-1 is a tool developed primarily for polarization tomography analysis of high Galactic latitudes, where the ISM is usually diffuse (e.g., D. Lenz et al. 2017), and the majority of the polarization is created in the nearby ISM (e.g., see A. Berdyugin et al. 2014; M. I. R. Alves et al. 2018). Therefore, the use of the inverse parallax as a proxy for stellar distance is justified if low-extinction stars have a high parallax SNR and their measured Gaia parallaxes are positive (C. A. L. Bailer-Jones et al. 2021; M. Fousneau et al. 2023). However, as we move closer to the Galactic thin disk, the inverse parallax becomes a poor distance estimate, especially for distant stars with a high column density, whose parallax SNR is often low (i.e., $d \gtrsim 2$ kpc, see Section 5.1). Consequently, the modeled distances of the clouds, derived using stellar parallax and polarization observations of the Galactic thin disk, are often overestimated and should be interpreted carefully. In Section 5.1, we propose a method to correct BISP-1's distance estimates in our samples. The correction is based on models of the inverse parallax–distance relation generated using our observations and photogeometric distance measurements from C. A. L. Bailer-Jones et al. (2021).

Furthermore, we show in Appendix A that faint red stars (those with $G > 18$ mag) have spurious parallax values. We give some possible explanations for this issue that affects only NIR observations. To avoid these unreliable measurements, we discard faint red stars with $G > 18$ mag for the polarization tomography analysis with BISP-1 using GPIPS data.

3.2. Gaussian Mixture Models

The Gaussian mixture model (GMM; G. J. McLachlan & K. E. Basford 1988) is a versatile probabilistic method used to represent a data set as a combination of a finite number of Gaussian distributions. The method estimates the mean, covariance, and mixing coefficients that best fit the data using the expectation–maximization (EM) algorithm.¹⁰ GMMs can

be particularly useful when the underlying data distribution is not well-defined or contains overlapping clusters.

We used the GMM method, implemented through the Scikit-learn Python library (F. Pedregosa et al. 2011), with optical and NIR starlight polarization, separately. We use the photogeometric distance and the normalized Stokes parameters $q_{(v, h)}$ and $u_{(v, h)}$ as the principal clustering features to find groups of sight lines sharing magnetic field properties. The three variables are normalized with the MinMax scaler tool.¹¹ GMM relies solely on these observables to identify groups, ignoring the uncertainties. Then, it assigns a label and membership probability to each element in the data set. The labels identify group members, allowing us to estimate the group's mean polarization properties and roughly determine the location of the polarizing clouds. This approach has been successfully applied by M. J. F. Versteeg et al. (2024) toward the Coalsack region, demonstrating multiple polarizing components along the LOS.

We tested four types of covariance (i.e., four mixture models): full, tied, diagonal, and spherical. These options offer flexibility in modeling the data. Their differences are described in Appendix C. The selection of the model and the number of Gaussian components is eased by the Bayesian information criterion (BIC; G. Schwarz 1978). The BIC is a statistical metric used for model selection among a group of potential models. It balances model fit and complexity by penalizing models with a higher component number. The lower BIC score represents the model that best captures the data patterns while avoiding overfitting. The number of clusters and the covariance model that minimizes the BIC in each case are presented in Table 3 (Appendix C). We ran the Scikit-learn GMM algorithm¹² with the parameters of Appendix C and the default Kmeans method to initialize the weights, the means, and the covariance.

4. Results

4.1. A One-to-one Comparison between the Optical and Near-infrared Polarization Measurements

We present a direct comparison between the optical and NIR measurements of stars that are common to both the IPS-GI and GPIPS data sets. To this end, we use the crossmatched polarization data sets (Section 2.4).

4.1.1. Optical-to-near-infrared Degree of Polarization Ratio

Figure 3 (top rows) shows the debiased optical and NIR polarization degree compared with the extinction density profiles as a function of distance from J. L. Vergely et al. (2022). The median and mean polarization degree per distance bin show consistent trends between the IPS-GI and GPIPS observations in the three studied regions. C5 exhibits the longest path lengths, compared to C45 and C50 (Figure 3). Both the optical and NIR degrees of polarization steadily increase throughout the entire LOS in C5 and C50. Contrarily, in C45, the optical and NIR polarizations remain roughly constant with distance.

The top row of Figure 4 presents the optical-to-NIR debiased polarization ratio (p_v/p_h) as a function of distance. Each bin contains approximately the same number of

¹⁰ EM is an iterative method to find (local) maximum likelihood estimates of parameters in statistical models.

¹¹ <https://scikit-learn.org/stable/modules/generated/sklearn.preprocessing.MinMaxScaler.html>

¹² <https://scikit-learn.org/stable/modules/mixture.html>

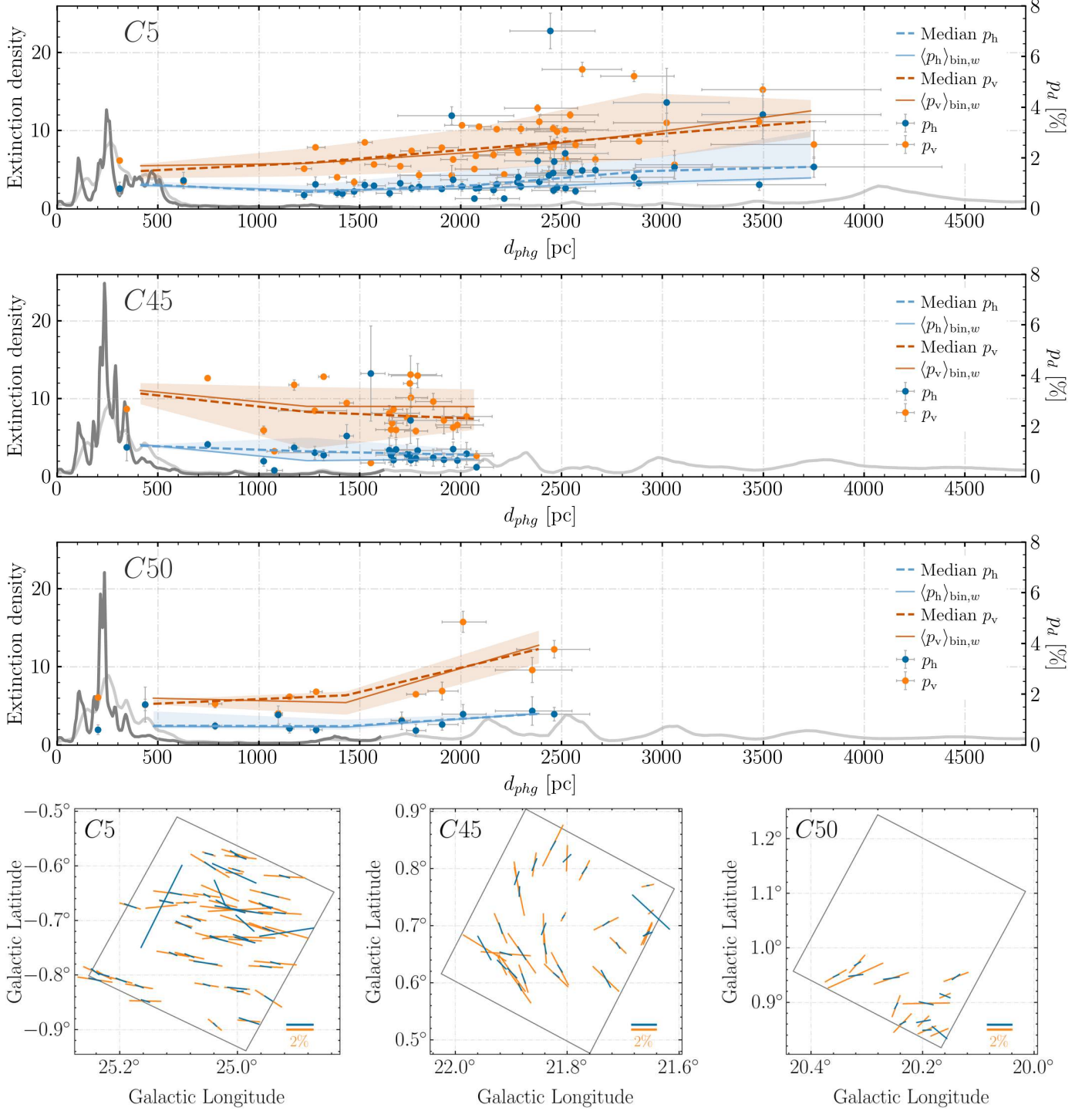


Figure 3. Optical (the orange dots) and NIR (the blue dots) debiased polarization degree as a function of the distance for stars common to both surveys in regions C5, C45, and C50 (from top to bottom, respectively). The dashed orange and blue lines show the median polarization degree, and the solid lines show the weighted mean per distance bin. The shaded areas represent the 68% confidence intervals. The polarization (right axis) is compared with optical extinction per parsec ($A_V \text{ pc}^{-1}$, left axis) from J. L. Vergely et al. (2022), at 10 pc (the solid gray curve) and 50 pc (the solid light-gray curve) resolution. The extinction density units are $10^{-3} \text{ mag pc}^{-1}$. Bottom row: polarization maps for stars common to IPS-GI (orange) and GIPS (blue) in the same regions. The gray squares mark the approximate limits of the IPS-GI field of view.

measurements, i.e., typically around 10 data points per bin. The average ratio of 2–3 observed in the three regions falls within the interstellar polarization expected from the Serkowski curve (K. Serkowski et al. 1975; see also M. J. F. Versteeg et al. 2025, in preparation) for typical values of the λ_{max} parameter (D. C. B. Whittet et al. 1992).

In general, variations in p_v/p_h could indicate different polarizing dust properties of the ISM structures sampled by both measurements, possibly revealing multiple clouds along the LOS (F. Patat et al. 2010). Additionally, the p_v/p_h ratio is sensitive to changes in dust extinction A_V , as shown by observations (e.g., D. C. B. Whittet et al. 1992, 2001;

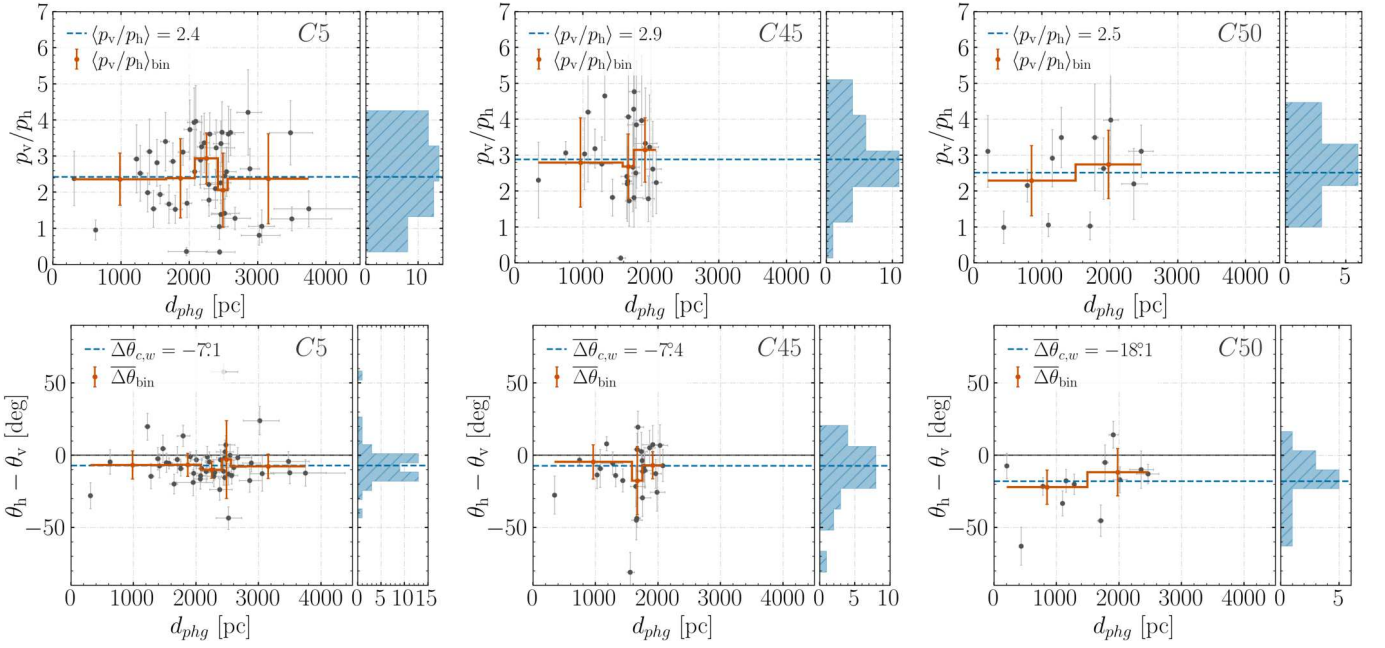


Figure 4. Top row: ratio of the degree of polarization in the optical to NIR as a function of distance of stars in common between the IPS-GI and GIPIS observations in each region. Bottom row: systematic difference between the NIR and optical polarization angles as a function of the distance in each region. The horizontal blue dashed line is the mean value of the distribution shown in the right-side panels. The solid dark-orange lines represent the mean and standard deviation per distance bin. The weighted circular mean and standard deviation were used in the case of the angular difference.

B. G. Andersson & S. B. Potter 2007), and grain alignment theory (A. Lazarian & T. Hoang 2007). However, the roughly constant ratios observed in Figure 4 (top row) suggest uniform polarizing dust properties along our sight lines. A few measurements with small errors and low p_v/p_h suggest a deviation from the expected average value in the ISM, but at rather low SNR.

4.1.2. Angular Alignment

Figure 3 (bottom row) shows polarization maps of the stars common to the IPS-GI and GIPIS catalogs. The optical and NIR polarization orientations are generally consistent within the errors. However, a few measurements show significant differences in polarization angles between wavelengths. A systematic polarization angle rotation with wavelength observed in individual clouds likely results from probing different depths (e.g., J. H. Hough et al. 1988), or from changes in grain size (S. Codina-Landaberry & A. M. Magalhaes 1976).

In general, the consistency in the orientation tells us that both observations trace similar polarizing properties of the structures within the regions studied, which is also evidenced through the optical-to-NIR degree of polarization ratio as a function of distance in Figure 4 (top row). Nevertheless, we also analyzed the systematic difference between the NIR and optical polarization orientations, defined as $\Delta\theta = \theta_h - \theta_v$ in the range $[-90^\circ, 90^\circ]$. Figure 4 (bottom row) presents $\Delta\theta$ as a function of distance in C5, C45, and C50. The right-side panels show the distribution of the angular difference along with the weighted circular mean (the dashed blue lines) calculated as

$$\overline{\Delta\theta} = \frac{1}{2} \text{atan2} \left[\frac{1}{W} \sum_{i=1}^N w_i \sin(2\Delta\theta), \frac{1}{W} \sum_{i=1}^N w_i \cos(2\Delta\theta) \right], \quad (3)$$

where w_i is the weight of the i th measurement calculated as $1/\sigma_{\Delta\theta,i}^2$, with $\sigma_{\Delta\theta}$ being the error of the angular difference

propagated from the observed errors as $(\sigma_{\theta_h}^2 + \sigma_{\theta_v}^2)^{1/2}$. W is the total sum of the weights.

We found a negative offset in $\overline{\Delta\theta}$ of $-7^\circ.1$, $-7^\circ.4$, and $-18^\circ.1$ in C5, C45, and C50, respectively. We used the reduced χ^2 to test the significance of the offset compared to a regression equal to zero in the angle difference. We used the relation

$$\chi_{\text{red}}^2 = \frac{1}{N-1} \sum_{i=1}^N \left(\frac{\Delta\theta_i - \overline{\Delta\theta}}{\sigma_{\Delta\theta,i}} \right)^2, \quad (4)$$

where N is the number of measurements and $\overline{\Delta\theta}$ is the average value (Equation (3)) or regression evaluated. First, we calculated the χ_{red}^2 of our best fits, obtaining values of approximately five, four, and three in C5, C45, and C50, respectively. Second, we calculated the χ_{red}^2 using $\overline{\Delta\theta} = 0$, that is, assuming that the difference in angle is zero, resulting in six, five, and eight for the three regions respectively. In C5 and C45, the two results are comparable and different from one. Therefore, we cannot conclude that there is a nonzero polarization orientation offset between optical and NIR observations. In C50, the χ_{red}^2 deviates more, with $\overline{\Delta\theta} = 0$ yielding the poorest regression fit, indicating a possible nonzero angle offset. However, in C50, the few common stars between the catalogs are more scattered, and the uncertainties are large. In conclusion, the χ_{red}^2 test indicates that the angular difference observed in the three regions does not deviate significantly from zero.

We divided the crossmatched data into distance bins to determine whether there are alignment variations at specific locations along the sight lines. The distance bins are defined as in the top row of Figure 4. Then, we calculated the weighted mean per bin with Equation (3), as shown by the solid dark-orange line in Figure 4, bottom row. The error bars are the weighted standard deviation of each bin. The weighted mean

of the systematic difference per distance bin does not show significant deviations from the total mean, represented by the horizontal dashed line in Figure 4 (bottom row), in any of the regions studied. Therefore, there is no significant correlation between the angle difference and the distance to the stars. Nevertheless, we emphasize that the big errors in the observations and the limited number of stars common between the catalogs prevent a more precise analysis.

4.2. Magnetic Field Tomography with BISP-1

Figure 5 presents the results of the polarization tomography using BISP-1 (Section 3.1) with high-quality optical and NIR data. The first and third rows show the polarization observations and the optical extinction density as a function of distance, along with BISP-1’s results. The three-cloud and four-cloud models best fit the optical observations, while the two-cloud model is the best solution for the NIR observations.

The second and fourth rows of Figure 5 show posterior distributions of the estimated cloud distances. In all cases, the nearest cloud distributions are broad due to the lack of zero-polarization measurements, leading to poorly constrained and prior-dominated solutions. Additionally, BISP-1’s minimum requirement of five stars between clouds (V. Pelgrims et al. 2023) contributes to poor constraints on second-nearest clouds in optical polarization, shifting distance posteriors toward lower values. The priors implemented in the modeling are detailed in Appendix B.

Table 1 summarizes the median LOS-integrated polarization degree, the circular mean magnetic field orientation on the plane of sky, and the median cloud distances (calculated as $1/\varpi$ from the median parallax posterior distribution) for each group of stars behind the clouds and each observed region. The reported uncertainties are derived from the spread in the posterior distributions and thus reflect model-based errors; see the notes in Table 1 for more details. Low-polarization components with large uncertainties have a biased median estimate due to p/σ_p ratios (where σ_p is the standard deviation of p) often falling below five. However, since we do not perform any further calculations using the LOS-integrated polarization degree, debiasing is unnecessary in this study. In the following sections, we analyze the tomography results for each region in detail.

4.2.1. C5

The best optical polarization model obtained for C5 using BISP-1 includes three polarizing layers at 116^{+20}_{-10} pc, 477^{+10}_{-10} pc, and $2.7^{+0.1}_{-0.1}$ kpc (Figure 5, left). The NIR polarization decomposition model showed two polarizing screens at 144^{+70}_{-30} pc and $2.88^{+0.1}_{-0.09}$ kpc, which are consistent within the uncertainties with the optical model. The median optical polarization degree increases gradually from $1.0^{+0.3}_{-0.3}\%$ behind the nearest cloud to $1.7^{+0.05}_{-0.05}\%$ and $2.5^{+0.1}_{-0.1}\%$ behind the intermediate and farthest clouds, respectively (Table 1). Meanwhile, the NIR polarization shows a smaller increase from $0.9^{+0.04}_{-0.04}\%$ to $1.1^{+0.04}_{-0.04}\%$.

The mean LOS-integrated optical polarization orientation (Figure 6, top) shifts significantly from $118^\circ \pm 10^\circ$ behind the first cloud to $77^\circ \pm 0^\circ.6$ behind the intermediate cloud and remains stable at $77^\circ\text{--}79^\circ$ beyond the distant layer, within a circular standard deviation of at most 1° . NIR polarization follows a similar trend, increasing from $67^\circ \pm 1^\circ$ to

$76^\circ \pm 1^\circ.2$ (Figure 7, top). While both orientations match beyond the distant cloud, they differ significantly after the nearby cloud due to the limited NIR measurements, which likely average the properties of the two clouds instead of just the nearest one.

4.2.2. C45

In C45, the optical polarization decomposition using BISP-1 identified four polarizing screens at 105^{+4}_{-4} pc, 476^{+40}_{-30} pc, 731^{+20}_{-40} pc, and $1.64^{+0.2}_{-0.07}$ kpc (Figure 5, middle), while NIR polarization decomposition revealed two clouds at 139^{+40}_{-30} pc and $2.2^{+0.1}_{-0.1}$ kpc. The nearby NIR cloud roughly agrees with the optical results, but, as with C5, significant uncertainties arise due to the limited number of nearby stars.

Beyond the near and first intermediate clouds, the LOS-integrated optical polarization remains around $0.9\%\text{--}1.1\%$, with uncertainties up to 0.4% (Table 1). It then increases to $2.0^{+0.2}_{-0.2}\%$ past the second intermediate cloud and decreases to $1.0^{+0.2}_{-0.2}\%$ after the farthest cloud. This trend likely reflects drastic changes in the magnetic field orientation along the LOS and across the observed field of view; for example, see the curved pattern present in each group of stars in Figure 6. The NIR polarization stays nearly constant at $0.7\%\text{--}0.8\%$, with an error of 0.1% , with no confirmation of the intermediate cloud.

The optical LOS-integrated polarization angle shifts significantly from $175^\circ \pm 10^\circ$ behind the near cloud (Figure 6, middle) to $49^\circ \pm 17^\circ$ behind the first intermediate layer, then to $33^\circ \pm 3^\circ$ and $7^\circ \pm 10^\circ$ beyond the second intermediate and distant clouds. The NIR polarization follows a different trend, changing from $33^\circ \pm 5^\circ$ nearby to $139^\circ \pm 3^\circ$ farther away (Figure 7, middle). Observations show a polarization angle distribution that broadens with distance behind virtually every cloud (Figures 6 and 7). The curved patterns, described by background stars, suggest complex, large-scale magnetic field structures that a single bivariate normal distribution with a simple mean orientation cannot fully represent. This complexity also limits the effectiveness of BISP-1 as it accounts only for polarization variations along the LOS.

4.2.3. C50

The four-cloud model is the best result for C50 using BISP-1 with optical polarization (Figure 5, right), identifying polarizing screens at 144^{+60}_{-30} pc, 478^{+40}_{-20} pc, $1.21^{+0.08}_{-0.06}$ kpc, and $2.31^{+0.04}_{-0.04}$ kpc. The NIR polarization decomposition showed two clouds at 141^{+50}_{-30} pc and $1.8^{+0.1}_{-0.1}$ kpc, with the near-cloud estimates aligning well with the optical results, but a 600 pc discrepancy in the distant cloud. This difference may be due to the limited NIR data coverage, as the GPIPS observations do not cover the entire C50 field of view (Figure 1), causing the optical and NIR to probe different ISM regions.

The $q_{(v, h)}$ and $u_{(v, h)}$ distributions as a function of distance show a significant change in polarization properties of the stars behind the distant layer, which are better defined in optical polarization. The median LOS-integrated optical polarization degree is higher in C50 than in the other regions, increasing gradually from $1.7^{+0.2}_{-0.2}\%$ to $3.5^{+0.1}_{-0.1}\%$ with distance (Table 1). In contrast, the NIR polarization is lower, ranging from $0.7^{+0.1}_{-0.08}\%$ to $1.0^{+0.05}_{-0.05}\%$.

The LOS-integrated polarization orientation changes significantly from one group of stars to another in the optical and NIR, except between intermediate clouds in the optical data,

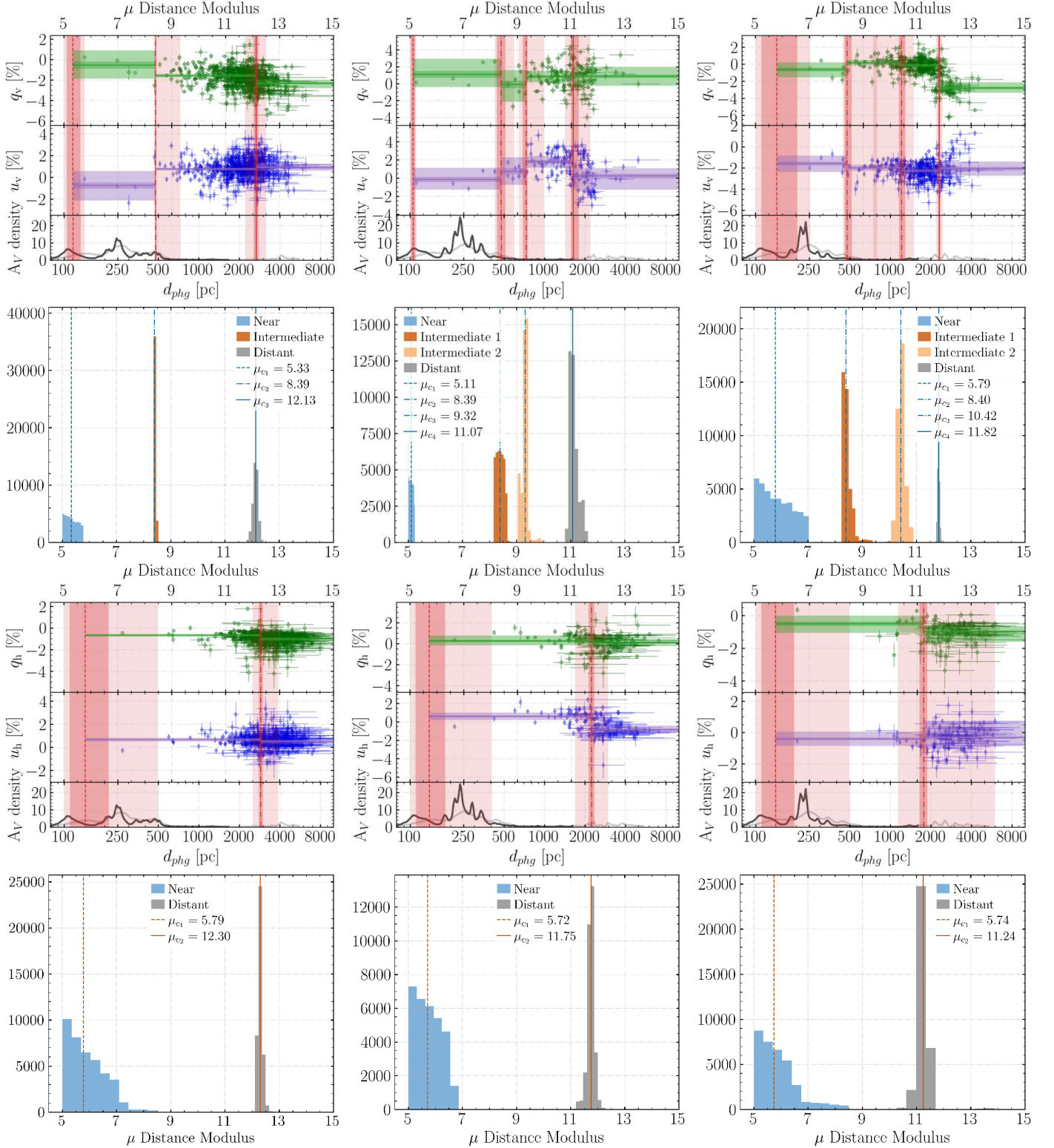


Figure 5. Best solutions of the polarization decomposition using BISP-1 with optical (first two rows) and NIR (last two rows) polarization observations in the regions of C5 (left), C45 (middle), and C50 (right). The first and third rows show the Stokes parameters $q_{(v, h)}$ and $u_{(v, h)}$ as a function of the distance modulus calculated using the inverse parallax. The red vertical lines and shaded areas represent the cloud median distances and their 1σ and 2σ confidence intervals. Similarly, the horizontal solid lines and shaded areas represent the LOS-integrated median $q_{(v, h)}$ (green) and $u_{(v, h)}$ (purple) and their 1σ and 2σ uncertainties for each group of stars behind the polarizing layers. The bottom panels show the extinction per distance unit (10^{-3} mag pc $^{-1}$) profiles from J. L. Vergely et al. (2022) at 10 pc (gray) and 50 pc (light-gray) resolution; the distance of the profiles is on a logarithmic scale. The vertical dashed lines show the median values. The second and fourth rows show the posterior distributions of the inverse parallax for each cloud modeled.

Table 1
Line-of-sight-integrated Polarization Properties as Derived From BISP-1 and Gaussian Mixture Model Modeling

Region	Cloud	BISP-1				GMM	
		p (%)	θ ($^\circ$)	$1/\varpi$ (kpc)	d_{phg} (kpc)	\bar{p} (%)	$\bar{\theta}$ ($^\circ$)
(1)	(2)	(3)	(4)	(5)	(6)	(7)	(8)
Optical Polarization							
C5	Near	$1.0^{+0.3}_{-0.3}$	118 ± 10	$0.116^{+0.02}_{-0.01}$	0.115	} 2.0 ± 0.5	78 ± 9
	Intermediate	$1.7^{+0.05}_{-0.05}$	77.0 ± 0.6	$0.477^{+0.01}_{-0.01}$	0.470		
	Distant	$2.5^{+0.1}_{-0.1}$	79.0 ± 1.0	$2.7^{+0.1}_{-0.1}$	2.4	3.3 ± 0.8	74 ± 10
C45	Near	$1.1^{+0.4}_{-0.3}$	175 ± 10	$0.105^{+0.004}_{-0.004}$	0.104	} 2.4 ± 0.9	36 ± 24
	Intermediate 1	$0.9^{+0.4}_{-0.3}$	49 ± 17	$0.476^{+0.04}_{-0.03}$	0.469		
	Intermediate 2	$2.0^{+0.2}_{-0.2}$	33 ± 3	$0.731^{+0.02}_{-0.04}$	0.714		
	Distant	$1.0^{+0.2}_{-0.2}$	7 ± 10	$1.64^{+0.2}_{-0.07}$	1.55	2.2 ± 1.0	164 ± 20
C50	Near	$1.7^{+0.2}_{-0.2}$	124 ± 4	$0.144^{+0.06}_{-0.03}$	0.143	} 2.1 ± 0.6	136 ± 11
	Intermediate 1	$2.0^{+0.08}_{-0.07}$	137.3 ± 1.2	$0.478^{+0.04}_{-0.02}$	0.471		
	Intermediate 2	$2.3^{+0.05}_{-0.05}$	133.2 ± 0.6	$1.21^{+0.08}_{-0.06}$	1.16	} 2.4 ± 0.6	134 ± 8
	Distant	$3.5^{+0.1}_{-0.1}$	108.2 ± 1.5	$2.31^{+0.04}_{-0.04}$	2.10		
NIR Polarization							
C5	Near	$0.9^{+0.04}_{-0.04}$	67.0 ± 1.2	$0.144^{+0.07}_{-0.03}$	0.143	1.2 ± 0.3	67 ± 10
	Distant	$1.1^{+0.04}_{-0.04}$	76.8 ± 1.2	$2.88^{+0.1}_{-0.09}$	2.55	1.6 ± 0.5	83 ± 18
C45	Near	$0.7^{+0.1}_{-0.09}$	33 ± 5	$0.139^{+0.04}_{-0.03}$	0.138	1.0 ± 0.4	22 ± 24
	Distant	$0.8^{+0.09}_{-0.1}$	139 ± 3	$2.2^{+0.1}_{-0.1}$	2.0	1.3 ± 0.4	138 ± 17
	2.2 ± 1.0	77 ± 18
C50	Near	$0.7^{+0.1}_{-0.08}$	110 ± 6	$0.141^{+0.05}_{-0.03}$	0.140	}
	Distant	$1.0^{+0.05}_{-0.05}$	99 ± 2	$1.8^{+0.1}_{-0.1}$	1.7		
						1.7 ± 0.6	81 ± 11

Note. Columns: (1) designation of the region; (2) polarizing cloud; (3) median polarization degree; (4) circular mean and standard deviation of the polarization angle; (5) median inverse parallax; (6) corrected photogeometric distance deduced from the models fitted to the observations (Section 5.1); (7) mean and standard deviation of the polarization degree; and (8) circular mean and standard deviation of the polarization angle. The parameters from columns (3) to (5) were calculated using the posterior distributions of $q_{(v, h)}$ and $u_{(v, h)}$, and ϖ obtained from BISP-1 decomposition (Section 3.1). The uncertainties of columns (3) and (5) are estimated from the 84th and 16th percentiles of the posterior distributions. The parameters of columns (7) and (8) were calculated for each component identified in the GMM clustering analysis (Section 3.2). The open brackets indicate correspondence with more than one component of the other method.

where the main difference is in the polarization degree (see the bottom rows of Figures 6 and 7, respectively). The optical polarization angles change from $124^\circ \pm 4^\circ$ behind the near cloud to $137.3^\circ \pm 1.2^\circ$ and $133.2^\circ \pm 0.6^\circ$ behind the intermediate clouds, and then to $108.2^\circ \pm 1.5^\circ$ behind the distant cloud. The NIR polarization follows a different trend, shifting from $110^\circ \pm 6^\circ$ in the nearby ISM to $99^\circ \pm 2^\circ$ farther away. The differences between the optical and NIR polarization may result from NIR field-of-view limitations and the potential averaging of multiple polarizing screens in the NIR near-cloud component.

4.3. Magnetic Field Tomography Using Gaussian Mixture Modeling

Figures 8, 9, and 10 present the clustering results with optical and NIR polarization in C5, C45, and C50, respectively. The solutions showed clear separation between Gaussian components in $q-u$ space, with most measurements having membership probabilities above $\sim 80\%$ and well-defined by distance (see Appendix C). We identified at least two components in each region, except for optical polarization in C50 and NIR polarization in C45, where we found three groups that best describe the different polarization properties

along the LOS and across the field of view. In the following sections, we present the GMM clustering results for each observed region. The average polarization properties are displayed in Table 1.

4.3.1. C5

We identified two main groups in the optical and NIR observations separately, using the GMM method (Figure 8). The approximate threshold of the farthest group agrees with the distant cloud obtained with BISP-1 using the optical and NIR observations (the vertical blue line). We increased the SNR cutoff limit to eight in the optical data and five in the NIR, sacrificing information from low-polarization measurements. This reduces the scatter and improves the clustering.

The mean optical polarization orientation of each group is consistent, within the dispersion, with the counterpart component in the NIR (Figure 8). Furthermore, although the nearest component of the clustering is expected to represent the combined contribution of the near and intermediate clouds found with BISP-1, the average polarization properties align more closely with those of the intermediate cloud alone (Table 1).

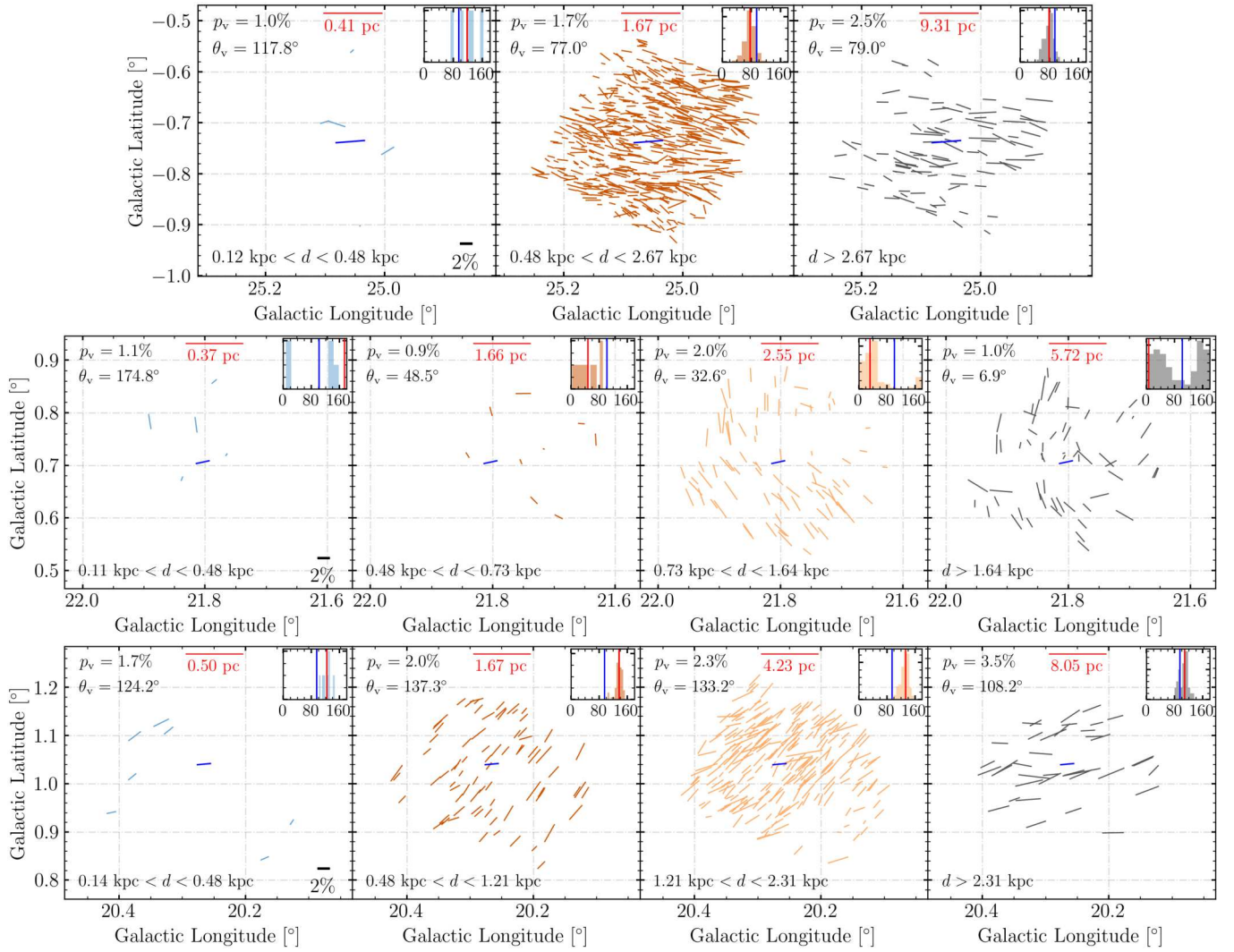


Figure 6. Polarization maps of star groups located behind each BISP-1 layer in C5 (top), C45 (middle), and C50 (bottom). The insets in the top right show the distribution of the polarization angle observed along with the median value (the red line) and the average magnetic field orientation from Planck (the blue line, also shown as a pseudovector in the center of the map). The median polarization properties of the components obtained with BISP-1 are shown in the top left of the panels (also see Table 1). The red ruler shows the actual spatial scale measured for an angular scale of $0^\circ 1$ at the distance of the clouds.

4.3.2. C45

The clustering of optical polarization in C45 yielded two components (Figure 9), which are consistent with the intermediate and distant components of the BISP-1 solution (Figure 5, middle). However, due to the low number of measurements in the nearby ISM, the clustering algorithm could not differentiate between the near and intermediate components identified by the BISP-1 decomposition, thus treating them as a single group.

On the other hand, the clustering with NIR polarization showed three groups in C45 (Figure 9, right). Two of these groups are closely related to variations of the polarization properties with distance and align with both optical polarization clustering (Figure 9, left) and the BISP-1 decomposition results (Figure 5, middle). The third group has different polarization properties across the field of view rather than along the sight line (Figure 9). Most measurements from this group are outside the IPS-GI field of view and observed distance range. Additionally, these measurements come from the faint red stars removed for the NIR polarization decomposition with BISP-1 (Appendix B).

4.3.3. C50

In C50, the optical polarization clustering resulted in three components (Figure 10, left). All three groups closely align with the two intermediate and the distant components obtained with BISP-1 (Figure 5, right). However, as in C45, the nearest component includes contributions from two different clouds, the near and intermediate clouds from the BISP-1 results. In the case of NIR polarization (Figure 10, right), there are very few nearby measurements. The majority of the NIR observations are beyond the known threshold of the distant cloud, 1.8 kpc (Table 1). As a result, the clustering does not recognize the nearest measurements as a separate group. Moreover, it seems to find a component even farther away than what optical polarization can detect. However, this additional polarization layer is not found with BISP-1 using the same observations. We attribute this discrepancy to either GMM failing to separate the components along the LOS due to the lack of nearby stars or to the presence of distant faint red stars, removed for the BISP-1 decomposition (Appendix A), which provide additional information at large distances in C50.

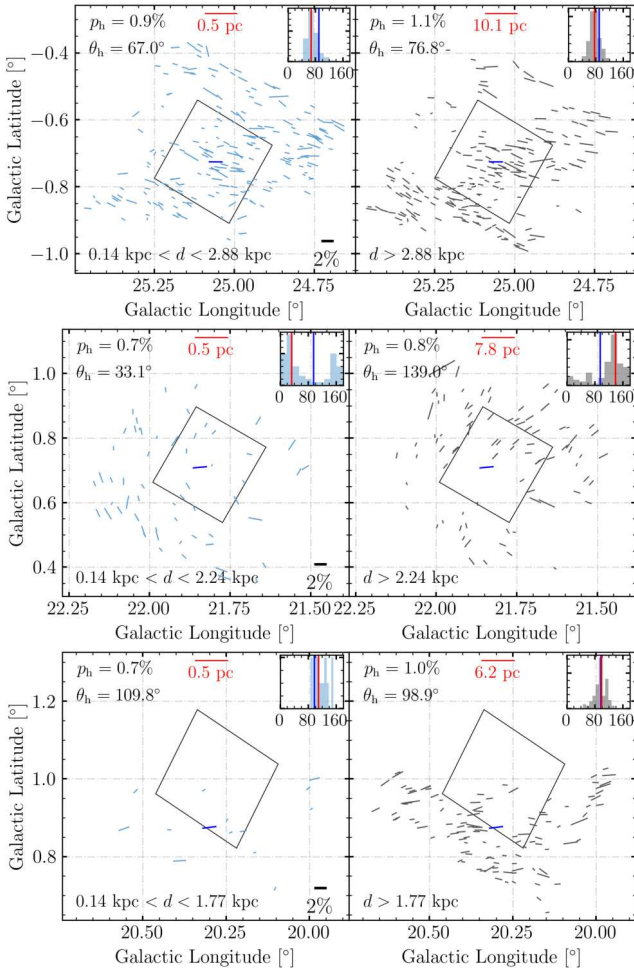


Figure 7. Same as in Figure 6 but using the NIR polarization observations. The black rectangle indicates the approximate location of the IPS-GI field of view.

5. Discussion

5.1. The Inverse Parallax–Distance Relation

The BISP-1 Bayesian algorithm relies on the Gaussian nature of the errors in the parallax to evaluate the probability of a star being in front of or behind a polarizing screen (V. Pelgrims et al. 2023). However, it is known that the inverse parallax is only a good approximation to the true stellar distance if the parallax SNR is high (C. A. L. Bailer-Jones et al. 2021; M. Fousneau et al. 2023). Furthermore, the least squares astrometric solution obtained from Gaia data processing can result in zero and negative observed parallaxes in the presence of measurement noise (X. Luri et al. 2018). Since the inverse parallax is constrained to be positive, negative parallaxes are an issue and should be discarded. These conditions are easily fulfilled in high-latitude regions, as V. Pelgrims et al. (2024) demonstrated. However, our regions are in the Galactic plane and have high column densities of the order of 10^{22} cm^{-2} (Figure 1). Additionally, several stars lie at large distances, resulting in low parallax SNR (Appendix A). Consequently, the inverse parallax is not a reliable estimate of the true stellar distance.

This is confirmed when comparing the photogeometric distances with the respective inverse parallaxes within each data set (Figure 11). The stellar photogeometric distances from

C. A. L. Bailer-Jones et al. (2021) are calculated using all Gaia photometry information alongside the parallaxes, thereby considering factors such as interstellar extinction. The validation of their solutions against independent distance estimates demonstrated that photogeometric distances are reliable up to several kiloparsecs (C. A. L. Bailer-Jones et al. 2021).

The gray solid line in Figure 11 indicates the linear inverse parallax–distance relation, from which the stars at $d \gtrsim 2 \text{ kpc}$ deviate significantly. A two-degree polynomial fit to the data weighted by the uncertainties describes the systematic deviation from the linear relation. We used the orthogonal distance regression method, which allowed us to include the uncertainties of both variables in the fitting. We used standard error propagation to calculate the inverse parallax errors as σ_{ϖ}/ϖ^2 . We performed 10,000 realizations with subsamples drawn without replacement from the measured data. The size of the subsamples was defined as $k = M - 200$, where M is the total number of measurements (~ 1800), including all objects observed in the optical and NIR across the three regions. The reduced χ^2 of the average best fit is presented in Figure 11. The average model allows us to relate the distance obtained from the tomography analysis with BISP-1 (i.e., $1/\varpi$) with the photogeometric distance. The corrected photogeometric distance values of each cloud are presented in Table 1.

5.2. A Comparison between Polarization Decomposition Methods

The GMM method clusters stars with similar polarization–distance properties but does not account for uncertainties. The polarization properties of each group are LOS integrated, and while distance information is used, separation by distance is not enforced. In contrast, BISP-1 decomposes the observed polarization to determine the intrinsic properties of individual clouds—only along the LOS—while considering ISM scatter and observational uncertainties. Additionally, BISP-1 provides LOS-integrated polarization properties for stars behind each cloud. In this paper, we directly compare BISP-1’s LOS-integrated component properties with the GMM method results with other ISM observations.

GMM performs well when the polarization data have a clear change with distance, as in C50, where polarization can be approximated as a bivariate distribution. However, GMM is less effective when the transition between components is very smooth or when the data scatter is large, as seen in C5. For instance, increasing the SNR threshold in optical and NIR polarization allowed the identification of at least two components along the LOS in C5, but low measurement density in some components can prevent proper group assignment, as in the nearby components. Furthermore, although clustering offers a way to separate the data set into groups with similar properties and assign a membership probability to each measurement, it cannot determine the distances of the polarizing clouds.

Nonetheless, GMM provides insights into magnetic field variations along the LOS and also seems to detect spatial variations of the field of view, tackling one limitation of BISP-1, e.g., the third group detected in C45 with NIR polarization (Figure 9). As seen in Figure 6 (bottom), some polarization pseudovectors in the second intermediate cloud have a similar orientation to those of the distant cloud, whereas in Figure 10 (bottom), the components are clearly separated.

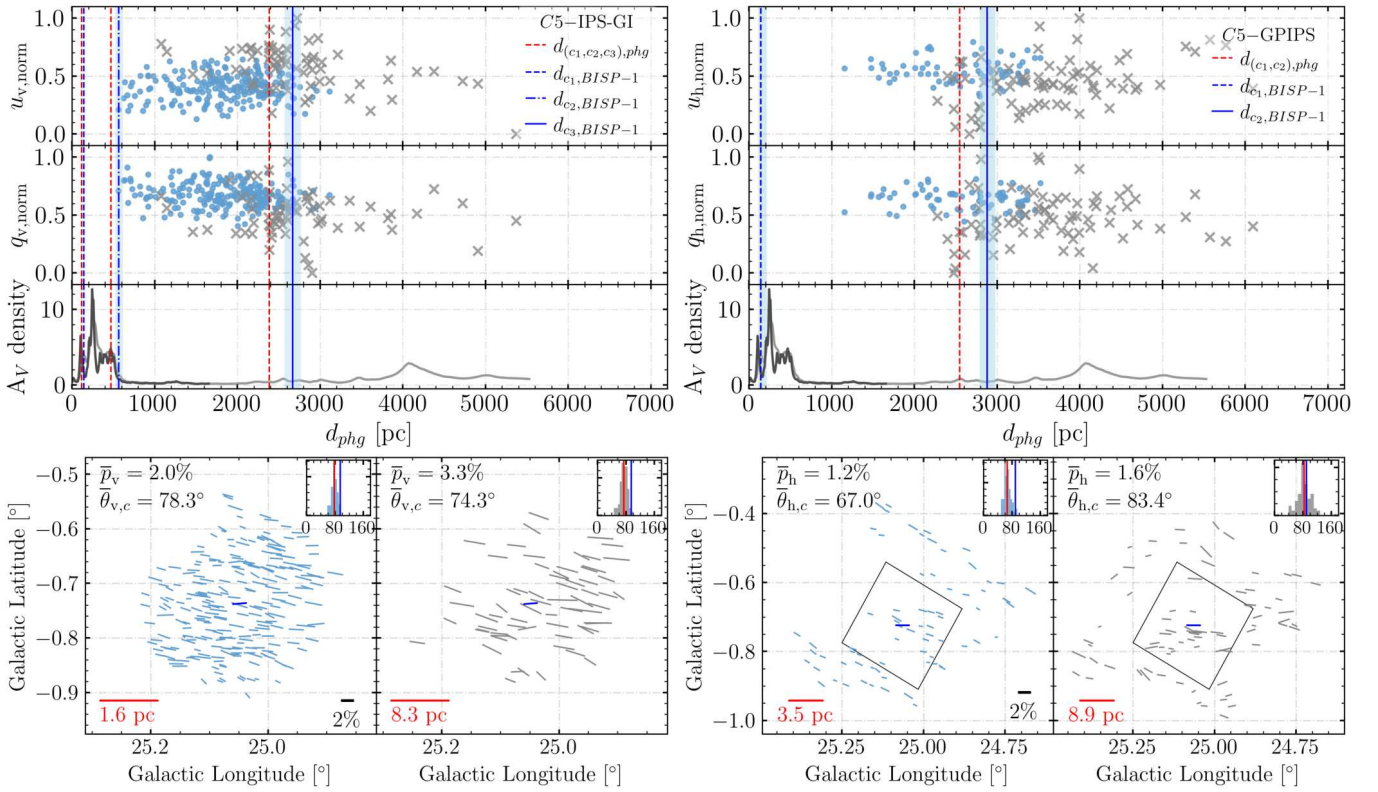


Figure 8. GMM results with optical (left) and NIR (right) polarization in C5. Top row: Stokes parameters $q_{(v, h)}$ and $u_{(v, h)}$ as a function of distance. The different colors and symbols represent the groups identified by the GMM. The extinction density with units of 10^{-3} mag pc $^{-1}$ from J. L. Vergely et al. (2022), at 10 pc (dark gray) and 50 pc (light-gray) resolution, is included in the bottom panel for comparison. The blue vertical lines show the location of the polarizing clouds identified with BISP-1; the red dashed vertical lines are the corresponding corrected distance (see Section 5.1). Bottom row: polarization orientation of stars in each cluster. The insets show the polarization angle distributions and the mean values (the red line). The black rectangle in the right panels indicates the approximate location of the IPS-GI field of view. The dark-blue pseudovectors represent the average orientation of the magnetic field within the region as observed by Planck.

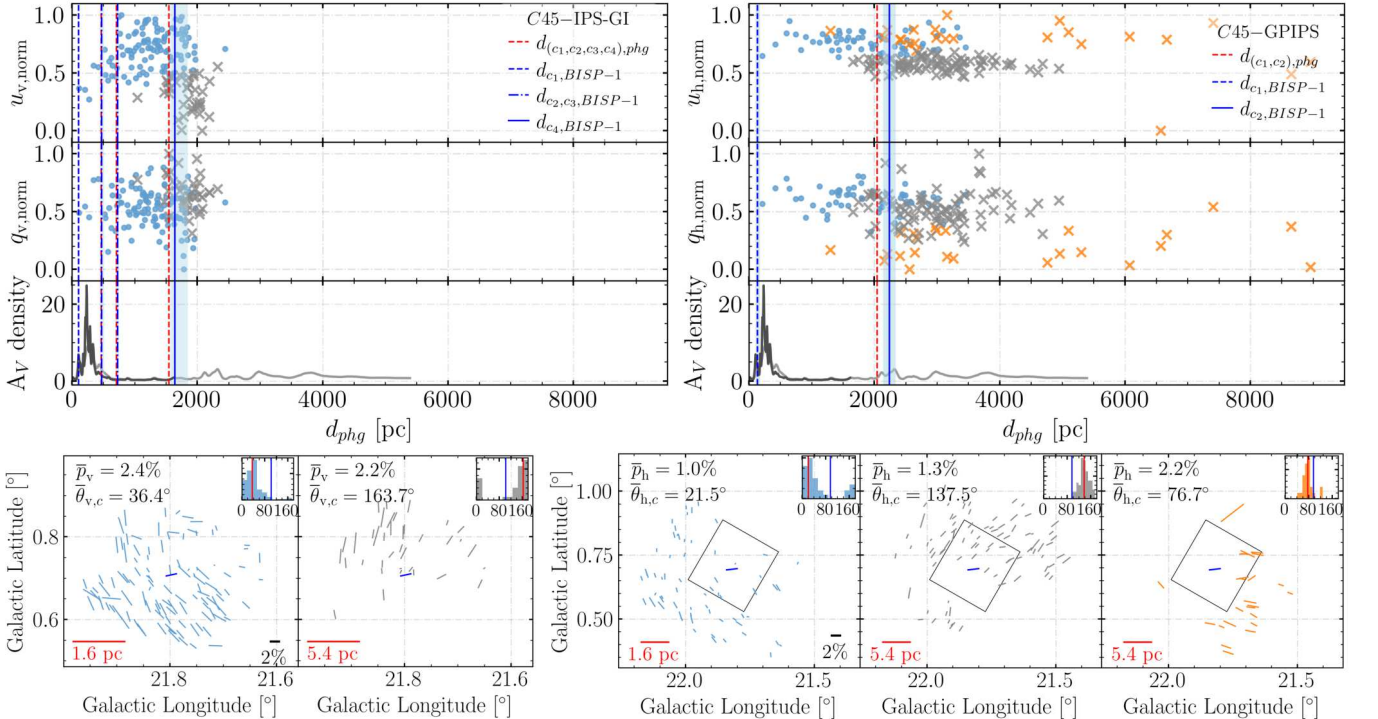


Figure 9. Same description as in Figure 8, but for C45.

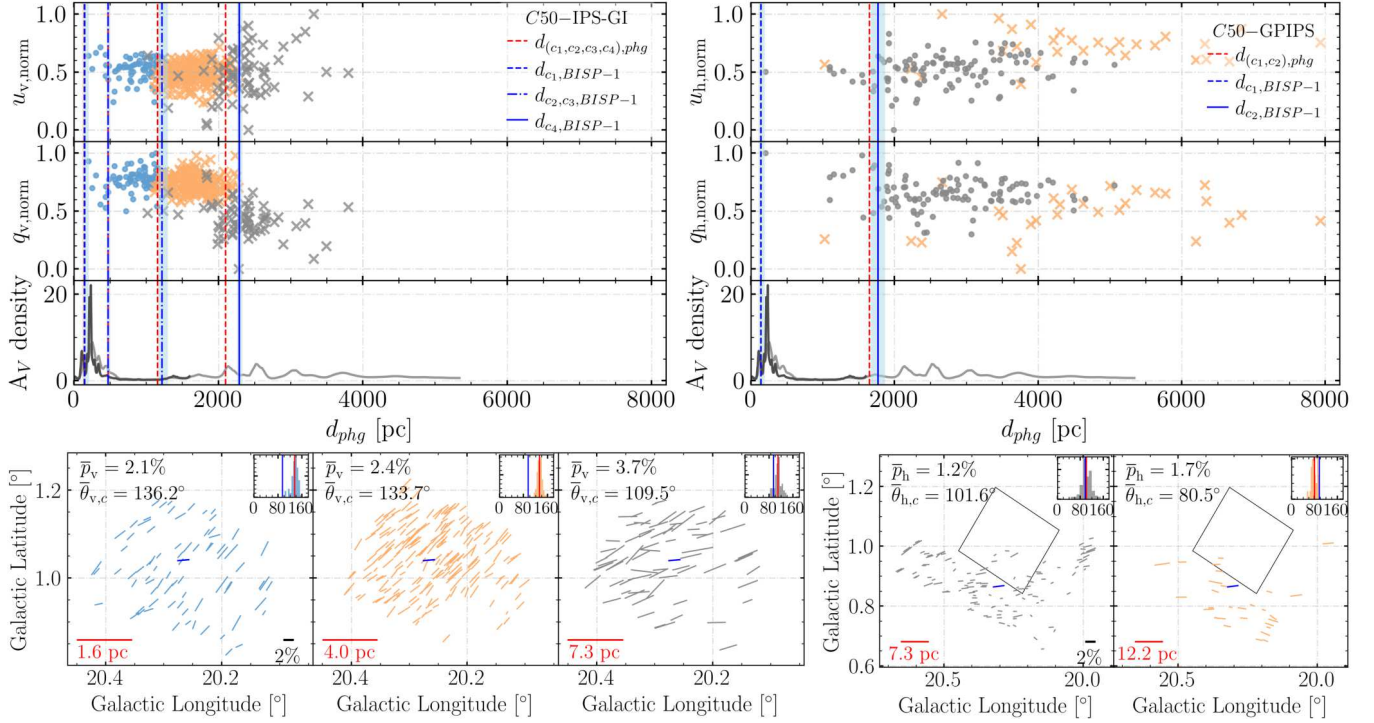


Figure 10. Same description as in Figure 8, but for C50.

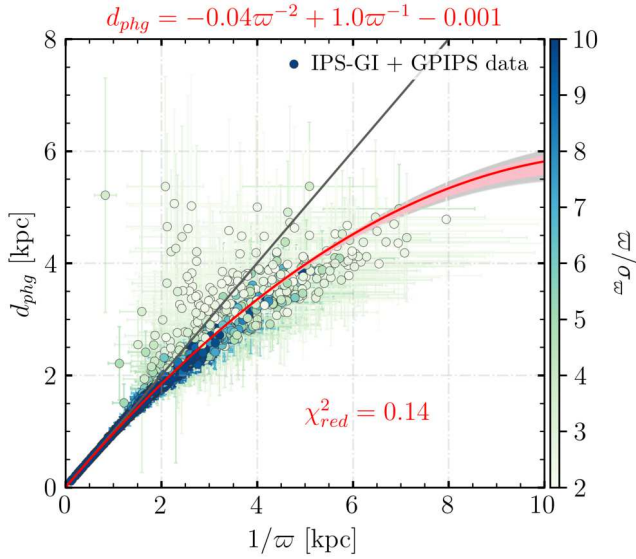


Figure 11. Photogeometric distances from C. A. L. Bailer-Jones et al. (2021) as a function of the inverse parallax of the stars observed by IPS-GI and GPIPS in the regions of C5, C45, and C50. The solid gray line indicates the expected inverse parallax–distance relation. The shaded pink area represents the best fits of subsamples drawn without replacement from the measured data. The solid red line is the average best fit of the subsamples. The gray shaded area is the 2σ confidence intervals.

This discrepancy arises from the sharp cutoff defined by the cloud’s distance in the BISP-1 decomposition and possibly from an inefficiency in detecting variations in the magnetic field properties across the field of view.

Furthermore, unlike BISP-1, we can use the photogeometric distances instead of the inverse parallaxes with GMM, which allows us to include the faint red stars in the NIR observations (Appendix A). Despite the difficulties of using clustering

algorithms and their lack of uncertainty handling, their solutions complement the Bayesian inference tomography results. With BISP-1, we can model the number of polarizing clouds and obtain their distances and average polarization properties alongside their uncertainties. Meanwhile, the GMM provides a method to separate the measurements into well-defined groups with different magnetic field properties along the sight line and possibly across the field of view as well. Together, these methods provide a robust picture of the plane-of-sky magnetic field properties.

5.3. Complex Magnetic Field Structure in C45

The curved pattern of the plane-of-sky magnetic field orientation is observed in all of C45’s components along the LOS, more clearly in the BISP-1 decomposition (e.g., see Figures 6 and 7) and perhaps also in Planck’s polarized emission (Figure 1). Low polarization with a random orientation is observed toward the northeast of the C45 field of view, suggesting a change in the magnetic field orientation, likely perpendicular to the plane of the sky. These patterns remain along the entire LOS, as observed by the optical and NIR polarization (e.g., see Figures 6, 7, and 9). The difference from one group of stars to another is the shift of the location of the low random polarization from the northeast to the southwestern part of the field of view.

This means that variations in magnetic field orientations happen primarily across the field of view, in addition to the LOS variations, explaining the depolarization observed. However, BISP-1 cannot accommodate this type of variation and, as a result, is unlikely to accurately determine the polarization properties of the intricate structures in the C45 region. On the other hand, GMM clustering seems to deal better with variations across the sky, as explained in Section 5.2. However, the intricate nature of the GMF in C45, showing large-scale variations in the plane-of-sky

orientation, could also challenge the performance of the GMM method, as it does not account for observed uncertainties.

Furthermore, a group of long sight lines observed within the C45 field of view in NIR exhibit a distinct plane-of-sky magnetic field orientation compared to the dominant patterns (Figure 9, right). These spatially localized measurements were detectable through the clustering method, which performs well when there are significant changes in polarization properties, not just along the LOS but also across the field, a feature that BISP-1 lacks. Moreover, most of these measurements originate from faint red stars, excluded in the BISP-1 analysis but retained during the clustering analysis. It is unclear what might lead to distinct magnetic field orientations in these particular sight lines. We speculate that it could be an elongated dust structure, such as a filament, within a distance not farther than 2 kpc (Figure 9, right).

5.4. Magnetic Field Properties across the Galactic Arms

5.4.1. Nearby Interstellar Medium or Local Arm

We found nearby polarizing clouds with both the optical and NIR observations. The optical observations better constrain the properties of the nearest clouds around 104 and 143 pc (Figure 5 and Table 1). This distance range agrees with the approximate location of the Local Bubble wall (R. Lallement et al. 2003; W. Liu et al. 2017; V. Pelgrims et al. 2020). High-resolution 3D dust maps have shown the presence of nearby dense and diffuse dust structures beyond and within the Local Bubble wall in a similar range of distances (R. H. Leike et al. 2020; J. L. Vergely et al. 2022; G. Edenhofer et al. 2024). The works of, for example, R. Skalidis & V. Pelgrims (2019) and V. Pelgrims et al. (2024) of high Galactic latitudes, Y. Angarita et al. (2024) of intermediate latitudes, B. G. Andersson & S. B. Potter (2005) and M. J. F. Versteeg et al. (2024) of the Coalsack region, and I. Medan & B. G. Andersson (2019) of the Local Bubble wall (at high latitudes) demonstrated that a large percentage of starlight polarization is produced in these nearby dust structures.

The intermediate polarizing screens observed with optical polarization are located between 470 and 714 pc. Figure 12 (bottom) shows the LOS-integrated G -band extinction as a function of distance, indicating that these intermediate clouds correspond to significant changes in stellar dust extinction. According to the high-resolution 3D dust maps (Figure 12, top), this distance range falls within the Local Arm. More specifically, the intermediate clouds may be linked to the southern structure of the Aquila Rift.

In NIR polarization, the intermediate clouds (in the Local Arm) are not detected in either method. This is likely because of the very low number of stars at distances at or in front of the Local Arm, which makes the distance determination of (nearby or intermediate) clouds very uncertain. NIR polarization from nearby stars (i.e., those crossing Local Bubble wall structures only) could be very low, causing fewer detections with low SNR.

5.4.2. Distant Interstellar Medium or Sagittarius Arm

The second intermediate cloud found at 1.16 kpc (Table 1) in C50 (Figure 5, right) is expected to be beyond the Local Arm, probably representing the transition between the interarm region and the Sagittarius Arm according to the 3D dust maps (Figure 12, top, and Figure 3, third row). Furthermore, the

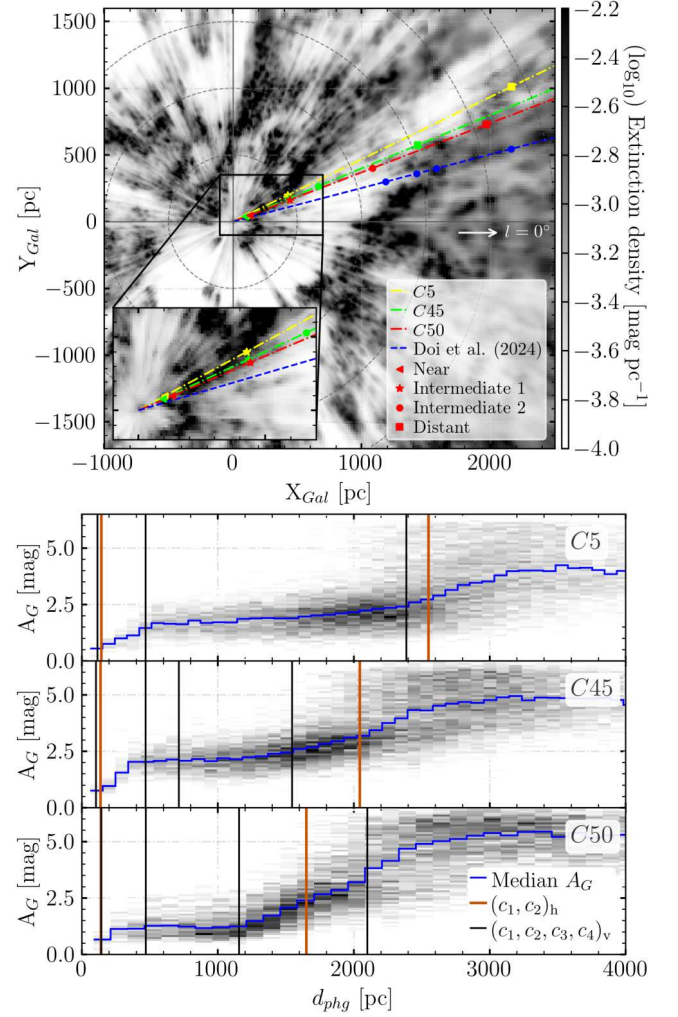


Figure 12. Top: LOSs of C5 (in yellow), C45 (in green), and C50 (in red) drawn over the extinction density XY plane from J. L. Vergely et al. (2022) at 10 pc ($d < 1.5$ kpc) and 25 pc ($d > 1.5$ kpc) resolutions. The markers indicate the adjusted positions of optical polarization clouds. Y. Doi et al. (2024)’s results for the Sagittarius Arm are displayed in blue for comparison. Bottom panels: G -band extinction from Gaia Collaboration et al. (2023) as a function of the photometric distance for all Gaia stars within C5 (top), C45 (middle), and C50 (bottom). The solid blue line is the median A_G per distance bin. The vertical lines show the polarizing screens identified with BISP-1 using the optical (black) and NIR (orange) observations, corrected for the bias in the inverse parallax–distance relation (Section 5.1).

distances to the farthest clouds are consistently traced by the optical and NIR polarization between 1.5 and 2.5 kpc, far beyond the Local Arm and within the Sagittarius Arm. These distance ranges align with the magnetic field tomography analysis by Y. Doi et al. (2024) of a region close to C50 (Figure 12, top).

The location of the second intermediate cloud in C50 matches that identified by Y. Doi et al. (2024) as their second component at 1.23 kpc in the Sagittarius Arm. Moreover, the mean magnetic field orientation of 134.5° in their foreground component, likely including contributions from various structures, aligns with the average orientation of 130° between the clouds of the Local Arm in C50 (Table 1).

The distance between the intermediate and distant clouds is larger in C5 than in the other regions. This could indicate that C5 has longer path lengths in the interarm region. This is in agreement with the extinction density profiles of Figure 3 and

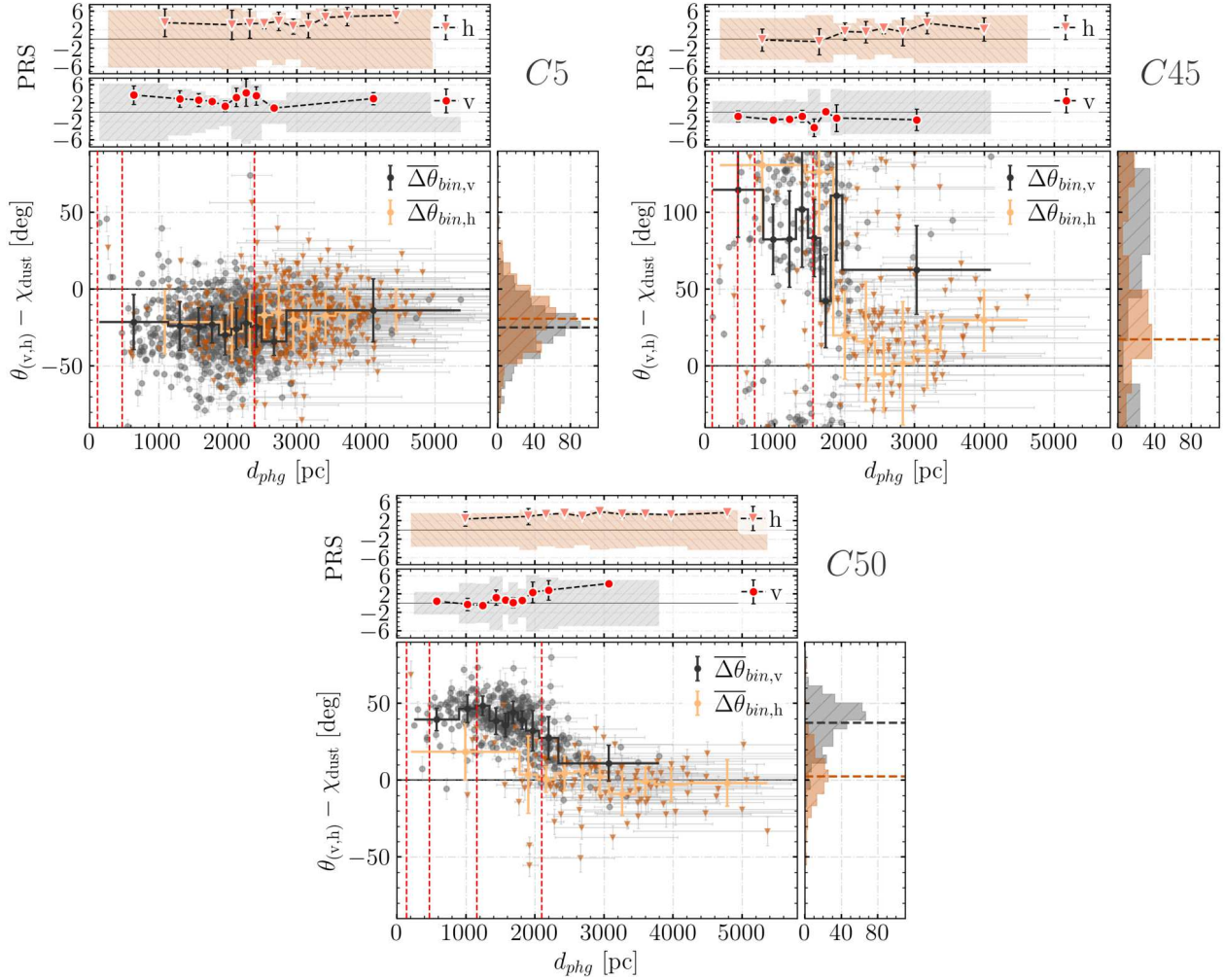


Figure 13. Magnetic field orientation difference between the starlight polarization and polarized thermal dust emission from Planck Collaboration XII et al. (2020) as a function of distance in C5 (top left), C45 (top right), and C50 (bottom). Due to the π ambiguity, the angular difference range in C45 was shifted by 50° for visualization. For each region, the bottom panels show the weighted circular mean difference per distance bin using the NIR (the solid light-orange) and optical (the solid black) observations. The error bars are the weighted circular standard deviation on each distance bin. The vertical red dashed lines show the corrected distance of the polarizing clouds found with BISP-1. The right-side panels show the angular difference distributions with the circular means (the horizontal dashed lines). The two top panels show the projected Rayleigh statistic (PRS; Equation (6)) per distance bin along with the weighted error. The gray and orange shaded areas represent the values between the maximum and minimum PRS per distance bin (see explanation in Section 5.5).

the stellar G -band extinction of Figure 12 (bottom) as a function of distance. The G -band extinction also aligns well with the distant clouds, although sampling issues in the NIR observations toward C50 seem to affect the accuracy of the distant cloud’s inferred location.

5.5. Magnetic Field Orientation Comparison between Starlight Polarization and Polarized Thermal Dust Emission

Planck’s 353 GHz polarized thermal dust emission may be depolarized beyond a certain distance because the larger beam averages over large-scale magnetic field variations (Planck Collaboration XII et al. 2020). This phenomenon, known as polarization horizon (B. Uyaniker et al. 2003), limits the observed path length to less than the full Galactic disk. Comparing Planck data with optical–NIR stellar polarization helps locate this horizon.

Figure 1 shows the plane-of-sky GMF orientation from starlight polarization (white and black pseudovectors, Section 2) and polarized thermal dust emission at 353 GHz from Planck (white texture), rotated by 90° . Overall, the

magnetic field orientations from the optical, NIR, and thermal dust observations partially align in the three regions, although some discrepancies exist between the optical–NIR and Planck data. Notably, Planck’s average magnetic field orientation (see blue pseudovectors of Figures 6 and 7) aligns better with the longest starlight polarization sight lines, which is expected given that Planck captures longer path lengths in the Galaxy.

For a quantitative comparison, we interpolated Planck’s values at each star’s position and computed the difference between the magnetic field orientations inferred from the starlight polarization and polarized thermal dust emission ($\theta_{v, h} - \chi_{\text{dust}}$, Figure 13). We calculated χ_{dust} using Planck’s High-Frequency Instrument processed maps at 353 GHz from Planck Collaboration III et al. (2020) as

$$\chi_{\text{dust}} = \frac{1}{2} \arctan 2(-U_{353}, Q_{353}) + 90^\circ, \quad (5)$$

where Q_{353} and U_{353} are the Stokes parameters in HEALPix’s COSMO convention (Planck Collaboration III et al. 2020). The negative sign converts χ_{dust} to the IAU (north-to-east)

convention. Uncertainties, $\sigma_{\chi_{\text{dust}}}$, are calculated following Equation (B.5) of Planck Collaboration Int. XIX et al. (2015). We used bilinear interpolation¹³ on the HEALPix Stokes parameters and covariance maps to obtain the values at each star's location.

In regions C45 and C50, the plane-of-sky GMF orientations differ significantly at near and intermediate distances (vertical lines in Figure 13 mark the polarizing clouds identified with BISP-1). However, the angular difference decreases to nearly zero beyond the distant clouds, as the orientations become increasingly aligned in the farthest stars, which are primarily those observed in the NIR (the orange triangles in Figure 13). Conversely, in C5, the angular difference is about -20° at all distances. This could be caused by dust at distances greater than what the starlight polarization can probe.

We tested the significance of the relative alignment using the PRS (D. Durand & J. A. Greenwood 1958), a metric often used to measure the alignment between linear polarization observations (e.g., D. L. Jow et al. 2018; G. V. Panopoulou et al. 2021, and references therein). The PRS statistic can discern between parallel (PRS > 0) or perpendicular (PRS < 0) alignments. We calculated the PRS and its weighted variance as in D. L. Jow et al. (2018):

$$\text{PRS} = \frac{1}{\sqrt{\sum_i^N w_i^2/2}} \sum_i^N w_i \cos(2\Delta\theta_i), \quad (6)$$

where $\Delta\theta_i = \theta_{(v, h), i} - \chi_{\text{dust}, i}$ is the angular difference of the i th value defined in the range $[-90^\circ, 90^\circ]$ and w_i is the weight defined as $1/\sigma_{\Delta\theta_i}^2$, with $\sigma_{\Delta\theta_i} = \sqrt{\sigma_{\theta_{(v, h), i}}^2 + \sigma_{\chi_{\text{dust}, i}}^2}$. The PRS depends on the number of measurements, N , in each distance bin. Therefore, we binned the data evenly and took care of the π ambiguity.

The top two panels of Figure 13 show the PRS values as a function of distance for each region and wavelength observed. The maximum and minimum values from Equation (6) correspond to the perfect parallel (i.e., $|\Delta\theta| = 0^\circ$) and perpendicular (i.e., $|\Delta\theta| = 90^\circ$) alignments, respectively, based solely on the measurement errors. The shaded areas represent possible value ranges due to the measurement errors. In C5, the PRS remains positive and fairly constant with distance but is not significantly higher than zero due to the large uncertainties, suggesting weak parallel alignment of the plane-of-sky magnetic field orientations. In C45 and C50, the PRS is negative in the near and intermediate polarizing clouds, mainly traced by optical polarization, indicating a misalignment in the structures of the Local Bubble wall and the Local Arm. Beyond 2 kpc, toward the Sagittarius Arm, parallel alignment becomes more significant, especially in C50, where the values are maximum and the error bars are very small.

In summary, the NIR observations in at least two regions are close to the maximum parallel alignment with Planck's magnetic field orientation, while the optical data often show little alignment, especially in C45 and C50. This indicates that the plane-of-sky magnetic field direction changes significantly along the LOS, at least in the Local Bubble wall and the Local Arm.

6. Summary

We presented a tomography analysis of the LOS-integrated plane-of-sky magnetic field component throughout the Galactic spiral arms based on optical and NIR starlight polarization observations of the Galactic plane in the regions named C5, C45, and C50. These LOSs probe the ISM structures in directions close to the Aquila Rift and the Sagittarius Arm. The high-quality optical and NIR observations consistently exhibit similar polarizing properties of the interstellar structures common to both observations, regardless of the number of these structures and their location along the LOS. Furthermore, the optical and NIR polarization data proved to be complementary, with the optical polarization better tracing the nearby ISM, while the NIR polarization primarily captures the distant ISM.

We determined the LOS-integrated polarization properties of the stars behind different magnetized dust clouds using two methods: the polarization decomposition tool BISP-1 and the GMM clustering tool. Both methods produced consistent results, particularly in the distant ISM (i.e., the Sagittarius Arm). Moreover, the information from each method is complementary: BISP-1 accurately locates the polarizing clouds and accounts for ISM scatter, while GMM clustering identifies large-scale magnetic field variations across the sky in addition to LOS variations and more effectively separates the star groups behind each cloud.

The polarization decomposition revealed three to four polarizing clouds along the LOS with optical observations and at least two with NIR data. The lack of NIR measurements with high SNR in the nearby ISM prevented us from finding the intermediate clouds observed with the optical polarization. Nevertheless, the distant stars observed in the NIR provided insights into the properties of the GMF and the ISM at greater distances than with the optical polarization. The near clouds between 104 and 143 pc are consistent with dust structures within the Local Bubble wall. The intermediate clouds around 469 and 714 pc are within the Local Arm. The second intermediate cloud in C50 at 1.16 kpc is beyond the Local Arm, as demonstrated by 3D dust maps from J. L. Vergely et al. (2022), and it is probably in the interarm region or the near edge of the Sagittarius Arm. Finally, the distant clouds between 1.5 and 2.5 kpc in the Sagittarius Arm are consistent with the results from Y. Doi et al. (2024). We emphasize that these values were obtained using solely starlight polarization and stellar distance information.

The starlight polarization tomography demonstrated large variations along the LOS of the plane-of-sky magnetic field properties in C45 and C50, from the Local Bubble wall to the Sagittarius Arm. This was also confirmed by comparing the starlight polarization with polarized thermal dust emission from Planck. The small difference in alignment observed in C5 along the entire LOS may be due to more dust observed by Planck farther away. Additionally, the magnetic field in C45 is complex and difficult to understand fully from the tomography analysis alone. Both methods consistently identified clouds along the LOS, but the curved magnetic field orientation and signs of depolarization between clouds suggest a complicated GMF structure across the Galactic arms, which both methods likely struggle to describe accurately. In conclusion, the above results show, first, the potential of using multiwavelength starlight polarization observations for Galactic tomography and, second, the need for complementary tomography tools or

¹³ <https://astropy-healpix.readthedocs.io/en/latest/interpolation.html>

the development of a new method that accounts for the intricate properties of the interstellar magnetic fields.

Acknowledgments

We would like to thank the anonymous referee for their valuable comments and suggestions, which have greatly improved the quality of this work. Over the years, IPS data have been gathered by a number of dedicated observers, to whom the authors are very grateful: Flaviane C. F. Benedito, Alex Carciofi, Cassia Fernandez, Tib erio Ferrari, Livia S. C. A. Ferreira, Viviana S. Gabriel, Aiara Lobo-Gomes, Luciana de Matos, Rocio Melgarejo, Antonio Pereyra, Nadili Ribeiro, Marcelo Rubinho, Daiane B. Seriacopi, Fernando Silva, Rodolfo Valentim, and Aline Vidotto. Y.A., M.H., and M.J.F.V. acknowledge funding from the European Research Council (ERC) under the European Union’s Horizon 2020 research and innovation program (grant agreement No. 772663). V.P. acknowledges funding from a Marie Curie Action of the European Union (grant agreement No. 101107047). C.V.R. acknowledges support from Conselho Nacional de Desenvolvimento Cient fico e Tecnol gico—CNPq (Brazil, grant 310930/2021-9), the Brazilian Ministry of Science, Technology and Innovation (MCTI), and the Brazilian Space Agency (AEB) by the support from PO 20VB.0009. A.M.M.’s work and optical–NIR polarimetry at IAG have been supported over the years by several grants from S o Paulo state funding agency FAPESP, especially 01/12589-1 and 10/19694-4. A.M.M. has also been partially supported by the Brazilian agency CNPq (grant 310506/2015-8). A.M.M.’s graduate students have been provided with grants over the years from the Brazilian agency CAPES. This research has used data, tools, and materials developed as part of the EXPLORE project, which has received funding from the European Union’s Horizon 2020 research and innovation program under grant agreement No. 101004214. Finally, this work has made use of data from the European Space Agency (ESA) mission Gaia (<https://www.cosmos.esa.int/gaia>), processed by the Gaia Data Processing and Analysis Consortium (DPAC; <https://www.cosmos.esa.int/web/gaia/dpac/consortium>). Funding for the DPAC has been provided by national institutions, in particular, the institutions participating in the Gaia Multilateral Agreement.

Facility: LNA:BC0.6m

Software: Astropy (Astropy Collaboration et al. 2013, 2018), Matplotlib (J. D. Hunter 2007), NumPy (C. R. Harris et al. 2020), SciPy (P. Virtanen et al. 2020), Scikit-learn (F. Pedregosa et al. 2011).

Appendix A Parallax of Faint Red Stars

The inverse parallax–distance relation of all high-quality Gaia observations in the regions studied revealed that the parallaxes of faint sources are biased. For example, Figure 14 presents the photogeometric distances (C. A. L. Bailer-Jones et al. 2021) as a function of the inverse parallax using all high-quality Gaia observations in the region of C5, colored by the parallax SNR. The red points show stars with spurious parallaxes and characterized by magnitudes above 18. Distant, faint stars are often assigned a large parallax, so they will erroneously appear as nearby sources (Figure 14, top). These sources are typically red stars (Figure 14, bottom). This is also

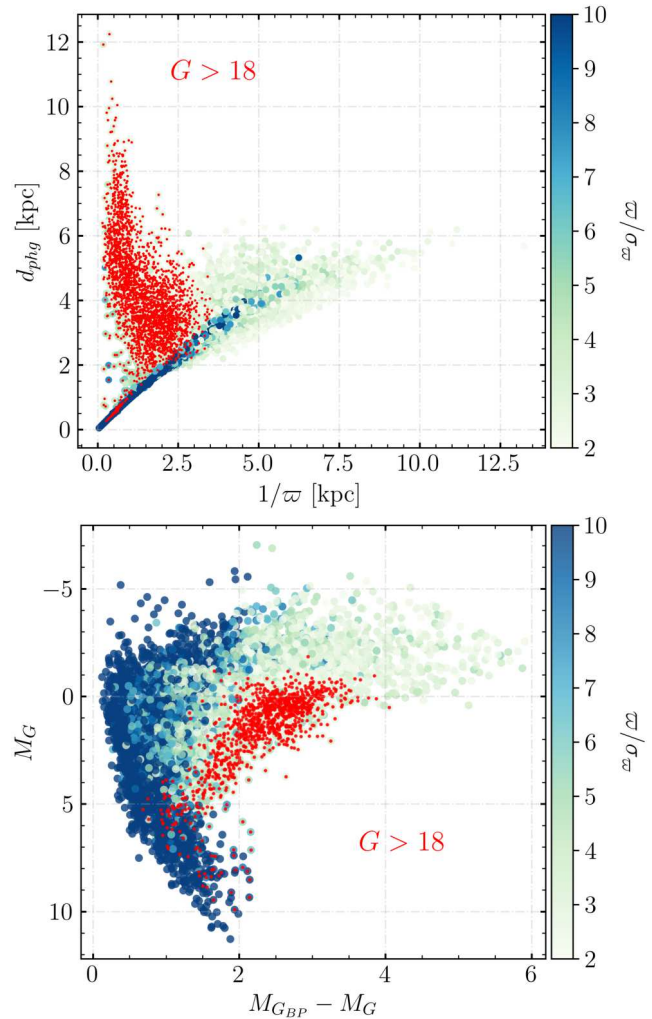


Figure 14. Top: comparison between the inverse parallax and the photogeometric distances from C. A. L. Bailer-Jones et al. (2021). Bottom: color–magnitude diagram from Gaia EDR3 photometry (Gaia Collaboration et al. 2021). Both panels present all high-quality Gaia measurements (i.e., $\varpi/\sigma_\varpi > 2$, $\text{RUWE} < 1.4$, and $\varpi > 0$) in the region C5, colored by the parallax SNR, which saturates at 10. The red points represent faint stars with $G > 18$.

observed with all high-quality Gaia data in the regions C45 and C50.

It is known that Gaia’s uncertainties in parallax, position, and proper motion increase significantly for faint stars (L. Lindgren et al. 2021a). Moreover, biased parallax measurements are a known issue reported for faint distant sources, such as quasars, and the solution to this issue is nontrivial (L. Lindgren et al. 2021b). Since BISP-1 relies on the parallax to perform the polarization decomposition along the LOS, spurious parallaxes from faint red sources represent an issue. To avoid this issue, we remove the faint stars with $G > 18$ when performing the polarization tomography with the GPIPS data set. This issue is not observed in the IPS-GI data set.

Appendix B Initial Parameters of the BISP-1 Decomposition

We present the priors used in the polarization decomposition with BISP-1 in Table 2. We followed the recipe of V. Pelgrims et al. (2023), primarily keeping the default values for most

Table 2
Limits of the Uniform Priors Used in the BISP-1 Polarization Decomposition

Region	Cloud	ϖ (mas)	$1/\varpi$ (pc)	q (%)	u (%)	C_{qq} (% ²)	C_{uu} (% ²)	C_{qu} (% ²)
(1)	(2)	(3)	(4)	(5)	(6)	(7)	(8)	(9)
Optical Polarization								
C5	Near	[2.00, 10.0]	[500.0, 100.0]	[-5.4, 5.4]	[-5.4, 5.4]	[0, 4]	[0, 4]	(-4, 4)
	Intermediate	[1.25, 3.33]	[800.0, 300.0]	[-5.4, 5.4]	[-5.4, 5.4]	[0, 4]	[0, 4]	(-4, 4)
	Distant	[0.161, 1.43]	[6219.2, 700.0]	[-5.4, 5.4]	[-5.4, 5.4]	[0, 1]	[0, 1]	(-1, 1)
C45	Near	[3.33, 10.0]	[300.0, 100.0]	[-4.7, 4.7]	[-4.7, 4.7]	[0, 2]	[0, 2]	(-2, 2)
	Intermediate 1	[1.67, 3.33]	[600.0, 300.0]	[-4.7, 4.7]	[-4.7, 4.7]	[0, 2]	[0, 2]	(-2, 2)
	Intermediate 2	[1.00, 2.50]	[1000.0, 400.0]	[-4.7, 4.7]	[-4.7, 4.7]	[0, 2]	[0, 2]	(-2, 2)
	Distant	[0.20, 0.83]	[4984.4, 1200.0]	[-4.7, 4.7]	[-4.7, 4.7]	[0, 3]	[0, 3]	(-3, 3)
C50	Near	[2.00, 10.0]	[500.0, 100.0]	[-6.2, 6.2]	[-6.2, 6.2]	[0, 1]	[0, 1]	(-1, 1)
	Intermediate 1	[1.25, 3.33]	[800.0, 300.0]	[-6.2, 6.2]	[-6.2, 6.2]	[0, 1]	[0, 1]	(-1, 1)
	Intermediate 2	[0.667, 1.43]	[1500.0, 700.0]	[-6.2, 6.2]	[-6.2, 6.2]	[0, 1]	[0, 1]	(-1, 1)
	Distant	[0.222, 1.00]	[4495.7, 1000.0]	[-6.2, 6.2]	[-6.2, 6.2]	[0, 2]	[0, 2]	(-2, 2)
NIR Polarization								
C5	Near	[2.00, 10.0]	[500.0, 100.0]	[-4.2, 4.2]	[-4.2, 4.2]	[0, 1]	[0, 1]	(-1, 1)
	Distant	[0.126, 3.33]	[7951.6, 300.0]	[-4.2, 4.2]	[-4.2, 4.2]	[0, 1]	[0, 1]	(-1, 1)
C45	Near	[2.00, 10.0]	[500.0, 100.0]	[-4.7, 4.7]	[-4.7, 4.7]	[0, 1]	[0, 1]	(-1, 1)
	Distant	[0.141, 3.33]	[7080.6, 300.0]	[-4.7, 4.7]	[-4.7, 4.7]	[0, 1]	[0, 1]	(-1, 1)
C50	Near	[2.00, 10.0]	[500.0, 100.0]	[-3.4, 3.4]	[-3.4, 3.4]	[0, 1]	[0, 1]	(-1, 1)
	Distant	[0.167, 3.33]	[5988.8, 300.0]	[-3.4, 3.4]	[-3.4, 3.4]	[0, 1]	[0, 1]	(-1, 1)

Note. Columns: (1) designation of the region; (2) polarizing cloud; (3) prior limits of the parallax; (4) the corresponding inverse parallax of the values in column (3); (5) and (6) the prior limits of the Stokes parameters $q_{(v, h)}$ and $u_{(v, h)}$, respectively; (7), (8), and (9) the elements of the intrinsic-scatter covariance matrix C_{qq} , C_{uu} , and C_{qu} , respectively.

parameters. Subsequently, we adjusted the distance and the diagonal elements of the intrinsic-scatter covariance matrix priors for each region in the sky. The lower limit of the distance prior for the nearest clouds was set at 100 pc following the approximate distance to the Local Bubble wall observed in the extinction density profiles of Figure 3 (see also R. Lallement et al. 2003; W. Liu et al. 2017; V. Pelgrims et al. 2020). The upper limit of the distance prior in the farthest clouds is set to the maximum observed distance by default. In all cases, we verified that the C_{qu} elements of the intrinsic-scatter covariance matrix fulfill their definition in the range $(-\sqrt{C_{qq}C_{uu}}, \sqrt{C_{qq}C_{uu}})$.

Appendix C

Initial Parameters and Validation of the Gaussian Mixture Model Clustering

The GMM package¹⁴ in the Scikit-learn Python library (F. Pedregosa et al. 2011) provides four fitting models based on the choice of the covariance matrix.

1. The full covariance type assigns a covariance matrix to each Gaussian component, meaning that each component can have its own shape and orientation in all dimensions.
2. A tied covariance indicates that all components have the same covariance, forcing all components to have the same shape and orientation.
3. The diagonal covariance type means that each Gaussian component has a diagonal covariance matrix, allowing

components to have different variances (i.e., shapes) and the same orientation along the coordinate axes.

4. The spherical covariance means that all elements of the diagonal covariance matrix are the same, assigning a single variance to each Gaussian component, which results in identical shapes and orientations along the axes.

A Gaussian distribution is defined by its covariance matrix and mean. The covariance determines the shape and orientation of the density distributions in all dimensions, while the mean specifies their location in space.

We tested each type of covariance model with different numbers of Gaussian components between one and nine. Table 3 presents the number of Gaussian components and the

Table 3

Parameters that Minimized the Bayesian Information Criterion in the Gaussian Mixture Model Clustering

Region	Optical			NIR		
	N	Cov. Model	BIC	N	Cov. Model	BIC
(1)	(2)	(3)	(4)	(5)	(6)	(7)
C5	2	spherical	-923.0	2	spherical	-274.0
C45	2	spherical	-155.6	3	diagonal	-566.0 ^a
C50	3	spherical	-1316.5	2	spherical	-324.5

Notes. Columns: (1) designation of the region; (2) and (5) the number of components; (3) and (6) the covariance model; (4) and (7) the minimum BIC number obtained with the parameters of the two columns on the right, respectively.

^a Second smallest BIC value. The minimum is -570.1.

¹⁴ <https://scikit-learn.org/stable/modules/mixture.html>

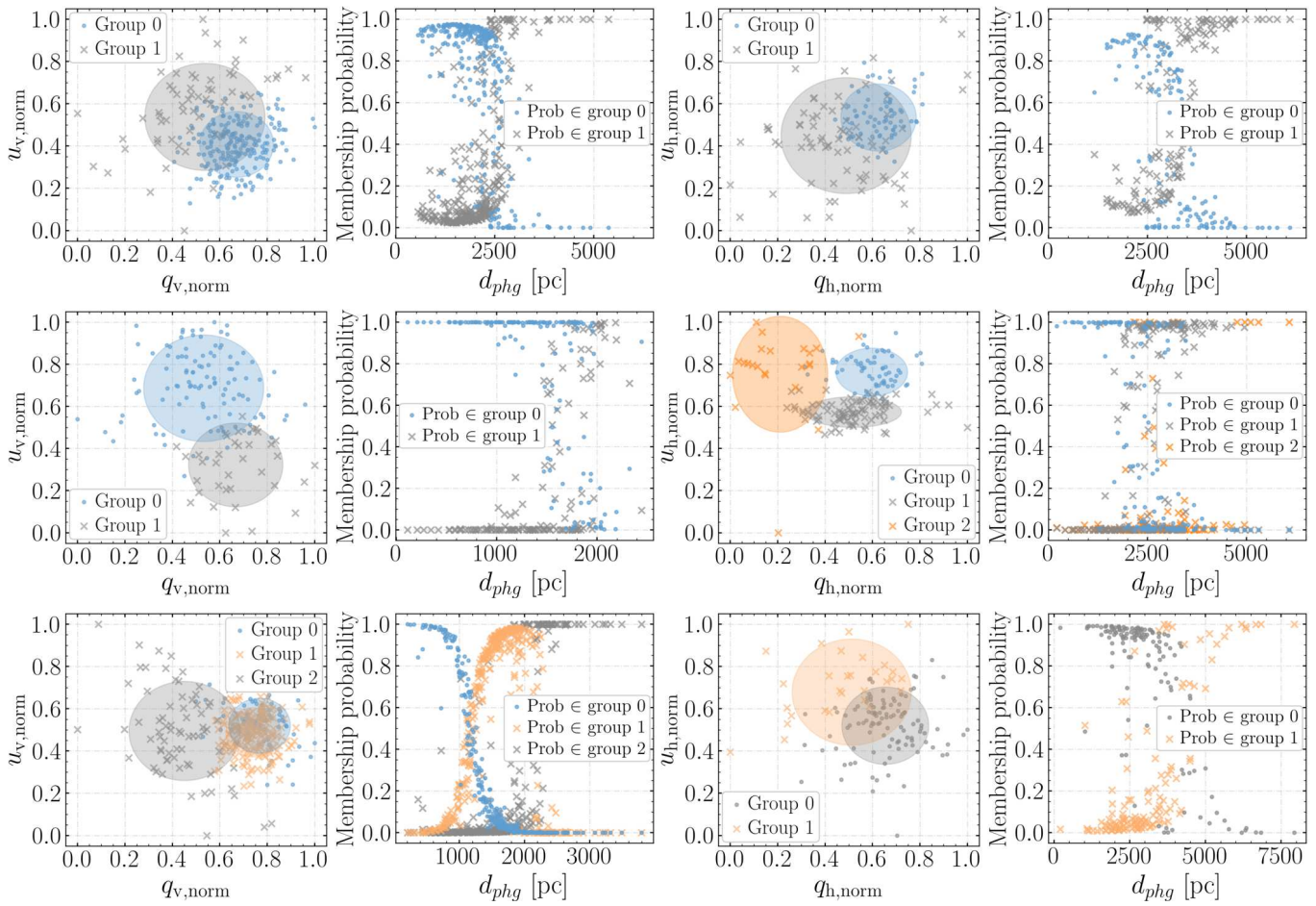


Figure 15. GMM results with optical (the two left columns) and NIR (the two right columns) polarization in C5 (top), C45 (middle), and C50 (bottom). The first and third columns are the group separations in normalized $q-u$ space. The ellipses represent the Gaussian components. The second and fourth columns are the group membership probability as a function of photogeometric distance. The colors correspond to the components of Figures 8–10.

covariance model that minimized the BIC in the GMM method for each data set. These parameters are subsequently used in the GMM clustering described in Section 4.3. For NIR polarization in C45, we chose the second-best option for the initial parameters (Table 3). This decision was made because the additional group consisted only of the four farthest measurements, which are too few to characterize any properties of the magnetic field. The same stars beyond 2.8 kpc were removed from the analysis with optical observation to improve the clustering, which can be affected by the contrasting long distances of these few measurements.

Figure 15 shows the group separation in $q-u$ space and the membership probability as a function of distance for each solution. The ellipses illustrate the 2D shapes and orientations of the individual Gaussian components obtained with the models in Table 3. We used the diagnostics of Figure 15 to confirm that the solutions obtained from the set of initial parameters minimizing the BIC (Table 3) were well-defined in $q-u$ space. Moreover, we ensured that the probabilities were above 80% in the majority of the measurements within each component (Figure 15).

ORCID iDs

Y. Angarita <https://orcid.org/0000-0001-5016-5645>
M. J. F. Versteeg <https://orcid.org/0000-0003-0400-8846>
M. Haverkorn <https://orcid.org/0000-0002-5288-312X>

V. Pelgrims <https://orcid.org/0000-0002-5053-3847>
C. V. Rodrigues <https://orcid.org/0000-0002-9459-043X>
A.M. Magalhães <https://orcid.org/0000-0002-1580-0583>
R. Santos-Lima <https://orcid.org/0000-0001-6880-4468>
Koji S. Kawabata <https://orcid.org/0000-0001-6099-9539>

References

- Akaike, H. 1998, in *Information Theory and an Extension of the Maximum Likelihood Principle*, ed. E. Parzen, K. Tanabe, & G. Kitagawa (New York: Springer), 199
- Alves, M. I. R., Boulanger, F., Ferrière, K., & Montier, L. 2018, *A&A*, **611**, L5
- Anders, F., Khalatyan, A., Queiroz, A. B. A., et al. 2022, *A&A*, **658**, A91
- Andersson, B. G., & Potter, S. B. 2005, *MNRAS*, **356**, 1088
- Andersson, B. G., & Potter, S. B. 2007, *ApJ*, **665**, 369
- Angarita, Y., Versteeg, M. J. F., Haverkorn, M., et al. 2023, *AJ*, **166**, 34
- Angarita, Y., Versteeg, M. J. F., Haverkorn, M., et al. 2024, *AJ*, **168**, 47
- Astropy Collaboration, Price-Whelan, A. M., Sipőcz, B. M., et al. 2018, *AJ*, **156**, 123
- Astropy Collaboration, Robitaille, T. P., Tollerud, E. J., et al. 2013, *A&A*, **558**, A33
- Bailer-Jones, C. A. L., Rybizki, J., Foesneau, M., Demleitner, M., & Andrae, R. 2021, *AJ*, **161**, 147
- Beck, R. 2003, arXiv:0310287
- Berdyugin, A., Piirola, V., & Teerikorpi, P. 2014, *A&A*, **561**, A24
- Berdyugin, A., Snare, M. O., & Teerikorpi, P. 1995, *A&A*, **294**, 568
- Beresnyak, A., & Lazarian, A. 2019, *Turbulence in Magnetohydrodynamics* (Berlin: De Gruyter)
- Cabral, B., & Leedom, L. 1993, *Special Interest Group on GRAPHics and Interactive Techniques Proceedings*, 263

- Clemens, D. P., Cashman, L. R., Cerny, C., et al. 2020, *ApJS*, **249**, 23
- Clemens, D. P., Pinnick, A. F., Pavel, M. D., & Taylor, B. W. 2012, *ApJS*, **200**, 19
- Codina-Landaberry, S., & Magalhaes, A. M. 1976, *A&A*, **49**, 407
- Doi, Y., Nakamura, K., Kawabata, K. S., et al. 2024, *ApJ*, **961**, 13
- Durand, D., & Greenwood, J. A. 1958, *JG*, **66**, 229
- Edenhofer, G., Zucker, C., Frank, P., et al. 2024, *A&A*, **685**, A82
- Ellis, R. S., & Axon, D. J. 1978, *Ap&SS*, **54**, 425
- Ferrière, K. 2015, *Journal of Physics Conference Series*, **577**, 012008
- Fosalba, P., Lazarian, A., Prunet, S., & Tauber, J. A. 2002, *ApJ*, **564**, 762
- Fouesneau, M., Frémat, Y., Andrae, R., et al. 2023, *A&A*, **674**, A28
- Fowler, L. A., & Harwit, M. 1974, *MNRAS*, **167**, 227
- Gaia Collaboration, Brown, A. G. A., Vallenari, A., et al. 2018, *A&A*, **616**, A1
- Gaia Collaboration, Brown, A. G. A., Vallenari, A., et al. 2021, *A&A*, **649**, A1
- Gaia Collaboration, Vallenari, A., Brown, A. G. A., et al. 2023, *A&A*, **674**, A1
- Green, G. M., Schlafly, E., Zucker, C., Speagle, J. S., & Finkbeiner, D. 2019, *ApJ*, **887**, 93
- Hall, J. S. 1949, *Sci*, **109**, 166
- Harris, C. R., Millman, K. J., van der Walt, S. J., et al. 2020, *Natur*, **585**, 357
- Hatano, H., Nishiyama, S., Kurita, M., et al. 2013, *AJ*, **145**, 105
- Haverkorn, M. 2015, in *Astrophysics and Space Science Library*, Vol. 407, *Magnetic Fields in Diffuse Media*, ed. A. Lazarian, E. M. de Gouveia Dal Pino, & C. Melioli (Berlin: Springer), 483
- Heiles, C. 1996, *ApJ*, **462**, 316
- Hiltner, W. A. 1949, *Sci*, **109**, 165
- Hough, J. H., Sato, S., Tamura, M., et al. 1988, *MNRAS*, **230**, 107
- Hunter, J. D. 2007, *CSE*, **9**, 90
- Jow, D. L., Hill, R., Scott, D., et al. 2018, *MNRAS*, **474**, 1018
- Lallement, R., Vergely, J. L., Babusiaux, C., & Cox, N. L. J. 2022, *A&A*, **661**, A147
- Lallement, R., Welsh, B. Y., Vergely, J. L., Crifo, F., & Sfeir, D. 2003, *A&A*, **411**, 447
- Lazarian, A., & Hoang, T. 2007, *MNRAS*, **378**, 910
- Leike, R. H., Glatzle, M., & Enßlin, T. A. 2020, *A&A*, **639**, A138
- Lenz, D., Hensley, B. S., & Doré, O. 2017, *ApJ*, **846**, 38
- Leroy, J. L. 1999, *A&A*, **346**, 955
- Lindegren, L., Bastian, U., Biermann, M., et al. 2021b, *A&A*, **649**, A4
- Lindegren, L., Klioner, S. A., Hernández, J., et al. 2021a, *A&A*, **649**, A2
- Liu, W., Chiao, M., Collier, M. R., et al. 2017, *ApJ*, **834**, 33
- Lloyd, S., & Harwit, M. O. 1973, in *Interstellar Dust and Related Topics*, ed. J. M. Greenberg & H. C. van de Hulst, 52 (Dordrecht: Springer), 203
- Luri, X., Brown, A. G. A., Sarro, L. M., et al. 2018, *A&A*, **616**, A9
- Magalhães, A. M., Pereyra, A., Melgarejo, R., et al. 2005, in *ASP Conf. Ser.* 343, *Astronomical Polarimetry: Current Status and Future Directions*, ed. A. Adamson et al. (San Francisco, CA: ASP), 305
- McLachlan, G. J., & Basford, K. E. 1988, *Mixture Models. Inference and Applications to Clustering* (New York: Marcel Dekker)
- Medan, I., & Andersson, B. G. 2019, *ApJ*, **873**, 87
- Nishiyama, S., Tamura, M., Hatano, H., et al. 2009, *ApJ*, **690**, 1648
- Panopoulou, G. V., Dickinson, C., Readhead, A. C. S., Pearson, T. J., & Peel, M. W. 2021, *ApJ*, **922**, 210
- Panopoulou, G. V., Tassis, K., Skalidis, R., et al. 2019, *ApJ*, **872**, 56
- Patat, F., Maund, J. R., Benetti, S., et al. 2010, *A&A*, **510**, A108
- Pattle, K., Fissel, L., Tahani, M., Liu, T., & Ntormousi, E. 2023, in *ASP Conf. Ser.* 534, *Protostars and Planets VII*, ed. S. Inutsuka et al. (San Francisco, CA: ASP), 193
- Pavel, M. D. 2014, *AJ*, **148**, 49
- Pavel, M. D., Clemens, D. P., & Pinnick, A. F. 2012, *ApJ*, **749**, 71
- Pedregosa, F., Varoquaux, G., Gramfort, A., et al. 2011, *JMLR*, **12**, 2825
- Pelgrims, V., Ferrière, K., Boulanger, F., Lallement, R., & Montier, L. 2020, *A&A*, **636**, A17
- Pelgrims, V., Mandarakas, N., Skalidis, R., et al. 2024, *A&A*, **684**, A162
- Pelgrims, V., Panopoulou, G. V., Tassis, K., et al. 2023, *A&A*, **670**, A164
- Planck Collaboration III, Aghanim, N., Akrami, Y., et al. 2020, *A&A*, **641**, A3
- Planck Collaboration Int. XIX, Ade, P. A. R., Aghanim, N., et al. 2015, *A&A*, **576**, A104
- Planck Collaboration Int. XLVIII, Aghanim, N., Ashdown, M., et al. 2016, *A&A*, **596**, A109
- Planck Collaboration XII, Aghanim, N., Akrami, Y., et al. 2020, *A&A*, **641**, A12
- Plaszczynski, S., Montier, L., Levrier, F., & Tristram, M. 2014, *MNRAS*, **439**, 4048
- Ramírez, E. A., Magalhães, A. M., Davidson, J. W. J., Pereyra, A., & Rubinho, M. 2017, *PASP*, **129**, 055001
- Schwarz, G. 1978, *AnSta*, **6**, 461
- Serkowski, K. 1962, *AdA&A*, **1**, 289
- Serkowski, K., Mathewson, D. S., & Ford, V. L. 1975, *ApJ*, **196**, 261
- Skalidis, R., & Pelgrims, V. 2019, *A&A*, **631**, L11
- Soler, J. D., Alves, F., Boulanger, F., et al. 2016, *A&A*, **596**, A93
- Uppal, N., Ganesh, S., Pelgrims, V., Joshi, S., & Sarkar, M. 2024, *A&A*, **690**, A49
- Uyaniker, B., Landecker, T. L., Gray, A. D., & Kothes, R. 2003, *ApJ*, **585**, 785
- Vergely, J. L., Lallement, R., & Cox, N. L. J. 2022, *A&A*, **664**, A174
- Versteeg, M. J. F., Angarita, Y., Magalhães, A. M., et al. 2024, *AJ*, **167**, 177
- Versteeg, M. J. F., Magalhães, A. M., Haverkorn, M., et al. 2023, *AJ*, **165**, 87
- Virtanen, P., Gommers, R., Oliphant, T. E., et al. 2020, *NatMe*, **17**, 261
- Whittet, D. C. B., Gerakines, P. A., Hough, J. H., & Shenoy, S. S. 2001, *ApJ*, **547**, 872
- Whittet, D. C. B., Martin, P. G., Hough, J. H., et al. 1992, *ApJ*, **386**, 562